NASA TECHNICAL NOTE

NASA TN D-6337

c. 1

NASA TN D-6337

EFFICIENCIES OF HONEYCOMB ABSORBERS OF SOLAR RADIATION

by E. M. Sparrow, William J. Bifano, and Jeanne A. Healy

Lewis Research Center
Cleveland, Ohio 44135

NATIONAL AERONAUTICS AND SPACE ADMINISTRATION • WASHINGTON, D. C. • MAY 1971

1. Report No.	2. Government Accession No.	3. Recipient's
NASA TN D-6337		

4. Title and Subtitle	5. Report Date
EFFICIENCIES OF HONEYCOMB ABSORBERS OF SOLAR RADIATION	May 1971
	6. Performing Organization Code
7. Author(s)	8. Performing Organization Report No.
E. M. Sparrow, William J. Bifano, and Jeanne A. Healy	E-6074
	10. Work Unit No. 120-33
9. Performing Organization Name and Address	11. Contract or Grant No.
Lewis Research Center National Aeronautics and Space Administration Cleveland, Ohio 44135	
	13. Type of Report and Period Covered
12. Sponsoring Agency Name and Address	Technical Note
National Aeronautics and Space Administration Washington, D.C. 20546	14. Sponsoring Agency Code

15. Supplementary Notes

16. Abstract

An analysis was made to determine the efficiency of solar energy absorption of a system consisting of a honeycomb structure affixed to a collecting base surface. For the study, it was assumed that the incoming solar radiation is perfectly collimated and impinges directly on the base surface. A two-band model (solar and infrared) was used in formulating the governing equations which account for simultaneous radiation and conduction. Honeycomb absorption efficiencies are presented for a range of radiation surface properties and dimensionless parameters involving honeycomb geometry, wall thermal conductivity, temperature level, and solar energy flux. In addition, the honeycomb efficiencies are compared to those of plane plate absorbers.

17. Key Words (Suggested by Author(s))	18. Distribution Statement
Auxiliary systems Thermodynamics Solar energy absorber	Unclassified - unlimited

19. Security Classif. (of this report)	20. Security Classif. (of this page)	21. No. of Pages	22. Price*
Unclassified	Unclassified	45	$3.00

*For sale by the National Technical Information Service, Springfield, Virginia 22151

EFFICIENCIES OF HONEYCOMB ABSORBERS OF SOLAR RADIATION

by E. M. Sparrow*, William J. Bifano, and Jeanne A. Healy

Lewis Research Center

SUMMARY

An analysis was made to determine the efficiency of solar energy absorption of a system consisting of a honeycomb structure affixed to a collecting base surface. A two-band model (solar and infrared) was used in formulating the integro-differential equations for simultaneous radiation and conduction energy transfer. Consideration was given to a wide range of radiation surface properties. Dimensionless parameters involving honeycomb geometry, wall thermal conductivity, temperature level, and solar energy flux were also varied over wide ranges. In the analysis, it was assumed that the honeycomb absorber is oriented such that the incoming solar radiation impinges directly on the base surface.

An extensive presentation of absorption efficiency results is made in graphical form. The efficiencies were found to be relatively insensitive to the specifics of the radiation surface properties, particularly in the range of higher efficiencies. This behavior stands in contrast to that of plane plate absorbers, which are highly sensitive to the surface properties. The honeycomb absorber thus might be considered for applications where surface degradation is likely to occur. Furthermore, in the range of higher efficiencies, the efficiency of a honeycomb absorber is also relatively insensitive to the values of the cavity geometrical and thermal parameters, thereby providing considerable latitude in design.

INTRODUCTION

The utilization of solar energy for certain space applications (e.g., solar thermoelectric converters, thermal control) requires a method of absorbing and retaining a large fraction of the incident solar radiation. In connection with such applications,

* Professor of Mechanical Engineering, University of Minnesota, Minneapolis, Minnesota.

spacecraft system designers typically consider either collecting surfaces with selective coatings (high solar absorptance, low infrared emittance) or solar concentrators which focus sunlight into a cavity absorber. Another technique, first suggested by Francia (ref. 1), is to place a honeycomb structure over the collecting surface (hereafter called the base surface of the honeycomb). Such a honeycomb would be designed to allow solar radiation to pass through to the base surface and to limit energy losses from the base due to emission and reflection.

The use of honeycombs to augment the collection of solar radiation has been examined, both analytically and experimentally, for terrestrial applications (refs. 2, 3, and 4). In these situations, the honeycomb is made from low thermal conductivity nonrefractory materials such as glass reinforced plastic.

A study conducted in 1968 (ref. 5) analyzed a titanium alloy honeycomb having blackened walls for space applications, the base surface also being black. The results of that analysis indicated that relatively good performance could be expected with the honeycomb absorber, even under conditions where selective coatings were known to degrade (e.g., high temperature, ultraviolet radiation, and micrometeorites).

The present investigation was undertaken to examine how the collection efficiency of a honeycomb absorber is affected by the radiation properties of the honeycomb walls and the base surface. In this connection, it may be anticipated that, owing to the multiple reflections that occur within a cavity, the honeycomb absorber should be less sensitive to radiation surface properties than plane surface absorbers. Correspondingly, the collection efficiency of honeycomb absorbers should be relatively less affected by surface degradation experienced during flight.

Consideration is given here to a wide range of radiation surface properties, including selective surfaces which have different properties in the solar and infrared ranges. From solutions of the governing integro-differential equations, an efficiency is evaluated as the ratio of the energy actually retained by the base surface to the energy of the incoming solar radiation. Results for the efficiency are presented as a function of dimensionless parameters which take account of honeycomb geometry and wall thermal conductivity as well as of the intensity of the solar radiation (i.e., distance from the Sun) and temperature level of the base surface. Particular emphasis is placed on the dependence of the efficiency on the radiation surface properties. The effect of honeycomb depth is also established. Throughout the analysis, it is assumed that the honeycomb absorber is oriented such that its axis is parallel to the incoming solar radiation. Comparisons are made between the efficiency results for honeycomb absorbers and those for plane surface absorbers.

In addition to the aforementioned major objective relating to the effects of radiation surface properties, two other aspects of honeycomb absorbers were considered in somewhat lesser depth. One of these has to do with the thermal boundary condition at the

exposed tips of the honeycomb walls. The second relates to the effect of severing conductive contact between the honeycomb and the base surface.

ANALYSIS

Description of the Problem

A typical portion of a honeycomb absorber is shown schematically in figure 1. Figure 1(a) is a full-face view, while figure 1(b) is a sectional view through A-A. The honeycomb is affixed to the base surface in a manner so as to ensure good conductive contact. The solar radiation arriving at the honeycomb is assumed to consist of parallel rays which are alined along the normal to the base surface. Also, the temperature of the base surface is postulated to be spatially uniform.

Owing to geometrical and thermal symmetry, there is no heat transfer across the midplane of the honeycomb walls as indicated by the dashed lines in figure 1(a). Therefore, from the standpoint of analysis, it is appropriate to consider the heat transfer problem for a single cavity bounded by side walls of thickness t and by the base surface.

Although it is possible, at least in principle, to solve the just-described radiative-conductive heat transfer problem, the required numerical computations would be very time consuming. The lengthy computational time results from the fact that the problem is governed by two-dimensional integro-differential equations. To bring the computations within tractable range while retaining the essential features of the problem, the analysis and solutions are carried out for a thin-walled circular cylindrical cavity as pictured in figure 2. The cavity has a depth L, a diameter d, and a wall thickness t. The outer surface of the cavity wall is adiabatic. The intensity of the solar radiation entering the cavity opening is denoted by q^s, which characterizes the solar energy per unit time and unit area. The base surface temperature is T_b. Axial distances are measured in terms of the coordinate x, with the origin of x being fixed at the open end of the cavity.

Formulation of the Governing Equations

As was mentioned in the INTRODUCTION, several models for the radiation surface properties are to be investigated. In the forthcoming paragraphs, the governing equations for the most general of these models will be formulated. The governing equations for the other models then follow as special cases. For all of the models considered herein, it is postulated that all participating surfaces are diffusely emitting and reflecting.

The most general characterization of the radiation surface properties to be considered here is a two-band model, with different properties for the base surface and for the cylindrical wall of the cavity. The two bands are, respectively, the solar band and the infrared band. In addition, it is assumed that the radiant energy emitted by the base and by the cylindrical wall is confined almost completely to the infrared, with a negligible contribution to the solar band.

Conductive-radiative energy balance. - The starting point of the analysis is an energy balance on a typical element of the cylindrical wall of the cavity, shown cross-hatched in figure 2(b). The element is ring-shaped and has surface area $dA_x = (\pi d)dx$. The energy balance involves both conductive and radiative contributions, that is,

$$\left(dQ_{net}\right)_{cond} + \left(dQ_{net}\right)_{rad} = 0 \tag{1}$$

If the temperature difference across the thickness of the wall is assumed to be negligible, then the conduction term is

$$\left(dQ_{net}\right)_{cond} = -k(\pi d)t\left(\frac{d^2T}{dx^2}\right)dx \tag{2}$$

The radiation term contains contributions from both the infrared and solar bands, each of which must be discussed separately.

Let B_c^{ir} denote the infrared radiation (superscript ir) leaving a surface element on the cylindrical wall (subscript c) per unit time and unit area (the quantity B is sometimes termed the radiosity). In general, B_c^{ir} will be a function of the axial coordinate x. The radiant flux leaving a surface element contains both emitted and reflected components, so that B_c^{ir} can be written as

$$B_c^{ir} = \epsilon_c^{ir}\sigma T_c^4 + \rho_c^{ir}H_c^{ir} \tag{3}$$

in which H denotes the radiation locally incident per unit time and area, and ϵ and ρ, respectively, denote the emittance and reflectance. The temperature T_c will, in general, vary with axial position along the cylindrical wall, as will H. Within the infrared band, the radiation properties are assumed to be gray, so that $\rho = 1 - \epsilon$ and equation (3) becomes (Symbols are defined in appendix A.)

$$B_c^{ir} = \epsilon_c^{ir}\sigma T_c^4 + \left(1 - \epsilon_c^{ir}\right)H_c^{ir} \tag{4}$$

The net radiant energy leaving an element is the difference between the leaving radiation and the incident radiation. In particular, for the infrared range,

$$\left(dQ_{net}\right)_{rad}^{ir} = \left(B_c^{ir} - H_c^{ir}\right) dA_x \tag{5}$$

After substitution of H_c^{ir} from equation (4), it follows that

$$\left(dQ_{net}\right)_{rad}^{ir} = \frac{\epsilon_c^{ir}}{1 - \epsilon_c^{ir}} \left(\sigma T_c^4 - B_c^{ir}\right) dA_x \tag{6}$$

A similar approach is used to derive the contribution of the solar band to the net radiation, with the one difference being that the emitted radiation is omitted. The end result is

$$\left(dQ_{net}\right)_{rad}^{s} = - \frac{\alpha_c^s}{1 - \alpha_c^s} B_c^s \, dA_x \tag{7}$$

in which α_c^s is the solar absorptance of the cylindrical wall.

When the energy balance, equation (1), is evaluated using equations (2), (6), and (7), and if dimensionless variables are introduced, there is obtained

$$\frac{d^2\theta}{dX^2} = N\left[\frac{\epsilon_c^{ir}}{1 - \epsilon_c^{ir}} \left(\theta^4 - \beta_c^{ir}\right) - \frac{\alpha_c^s}{1 - \alpha_c^s} \beta_c^s\right] \tag{8}$$

where

$$X = \frac{x}{d}, \quad \theta = \frac{T_c}{T_b}, \quad \beta = \frac{B}{\sigma T_b^4}, \quad N = \frac{\sigma T_b^3 \, d^2}{kt} \tag{9}$$

Equation (8) is a nonlinear ordinary differential equation for the dimensionless temperature distribution which contains, as additional unknowns, the radiosities $\beta_c^{ir}(X)$ and $\beta_c^s(X)$. Also appearing in the equation is the radiation-conduction parameter N.

To proceed with the formulation, it is necessary to provide boundary conditions for

θ and to derive additional equations for the radiosity functions β. With respect to the boundary conditions, it may be noted that temperature continuity at $x = L$ requires that $T_c = T_b$. Also, for small wall thicknesses, it appears reasonable to neglect the heat transfer from the exposed tip of the cylindrical wall (i.e., at $x = 0$). In terms of the dimensionless variables of the analysis, the boundary conditions may be stated as

$$\frac{d\theta}{dX} = 0 \text{ at } X = 0, \ \theta = 1 \text{ at } X = \frac{L}{d} \tag{10}$$

The influence of the boundary condition at $x = 0$ on the results will be examined later.

Radiosity equations. - Attention may now be turned to the governing equations for the radiosities β_c^{ir} and β_c^{s}. The former is defined by equation (4), the dimensionless form of which is

$$\beta_c^{ir} = \epsilon_c^{ir}\theta^4 + \left(1 - \epsilon_c^{ir}\right)\left(\frac{H_c^{ir}}{\sigma T_b^4}\right) \tag{11}$$

It remains to evaluate the incident radiant flux $H_c^{ir}/\sigma T_b^4$. Infrared radiation arrives at a ring element dA_x on the cylindrical wall from all other ring elements on the wall and from the base surface. The radiation arriving at dA_x from another wall element dA_ξ is

$$B_c^{ir}(\xi)dA_\xi \, dF_{\xi-x} \tag{12}$$

where $dF_{\xi-x}$ represents the angle factor for diffuse interchange between two ring elements. The algebraic representations for $dF_{\xi-x}$ and for all subsequent angle factors are given in appendix B. By integration of expression (12) over all elements dA_ξ and using the reciprocity rule for angle factors, one obtains the contribution of the cylindrical wall to $H_c^{ir}/\sigma T_b^4$

$$\int_{\xi=0}^{L/d} \beta_c^{ir}(\xi)dF_{X-\xi} \tag{13}$$

In evaluating the contribution of the base surface to $H_c^{ir}/\sigma T_b^4$, a simplifying assumption will be made, namely, that the base surface radiosity β_b^{ir} is spatially uniform. The motivation for incorporating this simplification is to help keep computational time within reasonable bounds. The consequences of this assumption are examined numerically in

appendix C, where it is shown to have an inconsequential effect on the results. Then, proceeding as in the prior paragraph, one finds the following contribution of the base to $H_c^{ir}/\sigma T_b^4$

$$\beta_b^{ir} F_{X-b} \tag{14}$$

in which F_{X-b} is the angle factor for diffuse interchange between a ring element and a disk.

When $H_c^{ir}/\sigma T_b^4$ in equation (11) is replaced by the sum of expressions (13) and (14), an integral equation for β_c^{ir} emerges

$$\beta_c^{ir}(X) = \epsilon_c^{ir}\theta^4(X) + \left(1 - \epsilon_c^{ir}\right)\left[\beta_b^{ir} F_{X-b} + \int_{\xi=0}^{L/d} \beta_c^{ir}(\xi) dF_{X-\xi}\right] \tag{15}$$

In addition to β_c^{ir}, equation (15) also contains the temperature distribution $\theta(X)$, which already appears in the energy balance (8), and another unknown β_b^{ir}. The latter is evaluated by noting that

$$B_b^{ir} = \epsilon_b^{ir}\sigma T_b^4 + \left(1 - \epsilon_b^{ir}\right) H_b^{ir} \tag{16}$$

and

$$H_b^{ir} = \frac{1}{A_b}\int_{x=0}^{L} B_c^{ir}(x) F_{x-b}\, dA_x \tag{17}$$

After the introduction of dimensionless variables and substitution of $dA_x/A_b = 4\, dX$, there is obtained

$$\beta_b^{ir} = \epsilon_b^{ir} + 4\left(1 - \epsilon_b^{ir}\right)\int_{\xi=0}^{L/d} \beta_c^{ir}(\xi) F_{\xi-b}\, d\xi \tag{18}$$

with ξ serving as the dummy variable of integration.

Then, the elimination of β_b^{ir} between equations (15) and (18) leads to

$$\beta_c^{ir}(X) = \epsilon_c^{ir}\theta^4(X) + F_{X-b}\epsilon_b^{ir}\left(1 - \epsilon_c^{ir}\right) + \left(1 - \epsilon_c^{ir}\right)\left[\int_{\xi=0}^{L/d} \beta_c^{ir}(\xi)dF_{X-\xi} + 4\left(1 - \epsilon_b^{ir}\right)F_{X-b} \times \int_{\xi=0}^{L/d} \beta_c^{ir}(\xi)F_{\xi-b}\,d\xi\right] \tag{19}$$

Equation (19) provides a means for evaluating the radiosity function β_c^{ir} which appears in the energy balance equation (8). Since θ and β_c^{ir} appear in both equations (8) and (19), it is necessary that they be solved simultaneously rather than successively.

The balance equation (8) also contains the radiosity β_c^S for the solar band. In the model employed here, the incoming solar radiation is envisioned as being directly incident on the base surface, where it is partially absorbed and partially reflected. A part of the thus-reflected radiation is incident on the cylindrical walls of the cavity, where further partial reflections occur; and so on and so forth. Further, it is postulated that the radiation emitted by the cavity surfaces contributes negligibly to the solar band.

In light of the foregoing paragraph, the radiosity β_c^S can be written as

$$\beta_c^S = \left(1 - \alpha_c^S\right)\left(\frac{H_c^S}{\sigma T_b^4}\right) \tag{20}$$

The contributions to $H_c^S/\sigma T_b^4$ are similar to those expressed by equations (13) and (14) for the infrared band, provided, of course, that the assumption of uniform base surface radiosity is retained. If equations (13) and (14) are used, with appropriate changes of notation, then equation (20) becomes

$$\beta_c^S(X) = \left(1 - \alpha_c^S\right)\left[\beta_b^S F_{X-b} + \int_{\xi=0}^{L/d} \beta_c^S(\xi)dF_{X-\xi}\right] \tag{21}$$

It remains to write an expression for the base surface radiosity β_b^S. The radiation incident on the base consists of directly arriving solar radiation as well as multiply-reflected solar radiation coming from the cylindrical walls. If proper account is taken of these contributions, then β_b^S is given by

$$\beta_b^s = \left(1 - \alpha_b^s\right)\left[\left(\frac{q^s}{\sigma T_b^4}\right) + 4 \int_{\xi=0}^{L/d} \beta_c^s(\xi) F_{\xi-b}\, d\xi\right] \tag{22}$$

which, when substituted into equation (21), yields

$$\beta_c^s(X) = F_{X-b}\left(1 - \alpha_c^s\right)\left(1 - \alpha_b^s\right)\left(\frac{q^s}{\sigma T_b^4}\right) + \left(1 - \alpha_c^s\right)\left[\int_{\xi=0}^{L/d} \beta_c^s(\xi) dF_{X-\xi} + 4\left(1 - \alpha_b^s\right) F_{X-b} \times \int_{\xi=0}^{L/d} \beta_c^s(\xi) F_{\xi-b}\, d\xi\right] \tag{23}$$

It is interesting to note that equation (23) is a self-contained integral equation for β_c^s, that is, it can be solved for β_c^s without recourse to any of the other governing equations. Thus, $\beta_c^s(X)$ can be determined prior to any consideration of the temperature distribution θ and the infrared radiosity β_c^{ir}. The intensity of the solar radiation enters the problem via the parameter $q^s/\sigma T_b^4$ that appears in equation (23).

Discussion of governing equations. - In view of the rather lengthy development that led to their derivation, it appears worthwhile to summarize the governing equations and the prescribable parameters. Also, some special cases will be deduced from the general formulation.

The three unknowns that emerge from the derivation are $\theta(X)$, $\beta_c^{ir}(X)$, and $\beta_c^s(X)$. Correspondingly, there are three equations (eqs. (8), (19), and (23)) plus the boundary conditions (10). Equation (23) is a linear integral equation which can be solved for β_c^s without recourse to the other equations and unknowns. The solution for β_c^s serves as input to equation (8). Equations (8) and (19) constitute a nonlinear integro-differential system for the coupled unknowns θ and β_c^{ir}. The solutions of the governing equations were obtained numerically. The techniques employed to carry out the solutions will be outlined in appendix D.

An inspection of equations (8), (10), (19), and (23) reveals the presence of the following prescribable parameters: N, L/d, $q^s/\sigma T_b^4$, ϵ_c^{ir}, α_c^s, ϵ_b^{ir}, and α_b^s, the last four of which are radiation surface properties. The parameter values employed in the numerical solutions will be indicated when the results are presented.

The governing equations for various special cases can be readily deduced from equations (8), (10), (19), and (23). For example, consider a model in which the participating surfaces are gray (i.e., $\epsilon_c^{ir} = \alpha_c^s = \epsilon_b^{ir} = \alpha_b^s \equiv \epsilon$). For this case, it is convenient to define

$$\beta_c = \beta_c^{ir} + \beta_c^{s} \tag{24}$$

Then, the sum of equations (19) and (23) becomes

$$\beta_c(X) = \epsilon\theta^4(X) + (1 - \epsilon)\left[F_{X-b}\epsilon + F_{X-b}(1 - \epsilon)\left(\frac{q^s}{\sigma T_b^4}\right) + \int_{\xi=0}^{L/d} \beta_c(\xi) dF_{X-\xi} + 4(1 - \epsilon)F_{X-b} \times \int_{\xi=0}^{L/d} \beta_c(\xi) F_{\xi-b}\, d\xi\right] \tag{25}$$

Further, in view of equation (24), the energy balance equation (8) takes the form

$$\frac{d^2\theta}{dX^2} = N\frac{\epsilon}{1 - \epsilon}\left(\theta^4 - \beta_c\right) \tag{26}$$

with boundary conditions expressed by equation (10). It is seen that the gray case is governed by a nonlinear integro-differential system for the coupled variables θ and β_c.

All other adaptations of the general formulation to the specific radiation properties considered herein are straightforward except, perhaps, for the case in which the cylindrical wall is a black surface. Since in this instance $\epsilon_c^{ir} = \alpha_c^{s} = 1$, $\beta_c^{ir} = \theta^4$, and $\beta_c^{s} = 0$, the right side of equation (8) is indeterminate. To avoid the indeterminancy, it is appropriate to repeat the derivation with ϵ_c^{ir} and α_c^{s} taken as unity at the outset. Alternatively, the governing equations may be retained as they stand and the black condition approximated by a value very close to one, for example, 0.998. Both approaches were employed, and it was found that any differences between the final results were completely imperceptible in the graphical presentation of results.

Efficiency and Apparent Emittance

The performance of the honeycomb absorber system will be characterized by an efficiency η defined as

$$\eta = \frac{\text{net rate of energy gain by base}}{\text{rate of arriving solar radiation}} \tag{27}$$

The numerator of equation (27) represents the excess of the energy gains over the energy losses at the base surface. It corresponds to the energy available for subsequent application. The energy gained by the base surface is due to the absorption of solar radiation, while the losses occur as a result of radiation and heat conduction. Thus, it may be expected that higher efficiencies will correspond to larger values of $q^s/\sigma T_b^4$.

If $A_o(=\pi d^2/4)$ is the area of the cavity opening, then the rate of arriving solar radiation is $q^s A_o$. With respect to the numerator of equation (27), it follows from an overall energy balance on the cavity that the net gain by the base surface is equal to the net rate at which radiant energy enters the cavity opening. Then, if Q_o denotes the rate at which radiation streams outward through the opening, the numerator is equal to

$$q^s A_o - Q_o \tag{28}$$

so that the efficiency is expressible as

$$\eta = \frac{q^s A_o - Q_o}{q^s A_o} = 1 - \frac{\left(\dfrac{Q_o}{A_o \sigma T_b^4}\right)}{\left(\dfrac{q^s}{\sigma T_b^4}\right)} \tag{29}$$

It is customary to define the apparent emittance of a cavity as

$$\bar{\epsilon} = \frac{Q_o}{A_o \sigma T_b^4} \tag{30}$$

so that

$$\eta = 1 - \frac{\bar{\epsilon}}{\left(\dfrac{q^s}{\sigma T_b^4}\right)} \tag{31}$$

It remains to express Q_o and $\bar{\epsilon}$ in terms of the functions provided by the solutions of the governing equations. From a typical surface element dA_x on the cylindrical wall of the cavity, the radiant energy passing out of the opening is

$$\left(B_c^{ir} + B_c^{s}\right) F_{x-o}\, dA_x \tag{32}$$

For all such elements, the contribution to Q_o is

$$\int_{x=0}^{L} \left(B_c^{ir} + B_c^{s}\right) F_{x-o}\, dA_x \tag{33}$$

Similarly, from the base surface, the outstreaming radiation is

$$\left(B_b^{ir} + B_b^{s}\right) F_{b-o} A_b \tag{34}$$

Summing equations (33) and (34) yields

$$\bar{\epsilon} = \frac{Q_o}{A_o \sigma T_b^4} = \left(\beta_b^{ir} + \beta_b^{s}\right) F_{b-o} + 4 \int_{\xi=0}^{L/d} \left(\beta_c^{ir} + \beta_c^{s}\right) F_{\xi-o}\, d\xi \tag{35}$$

It is seen from equation (35) that $\bar{\epsilon}$ is determined from the radiosities of the base surface and the cylindrical wall. Once $\bar{\epsilon}$ is evaluated from equation (35), then the efficiency η follows directly from equation (31).

The foregoing expression for $\bar{\epsilon}$ applies for all of the cases treated herein, although its form is somewhat different for various specific cases. For example, when the participating surfaces are gray, then $\beta_b^{ir} + \beta_b^{s}$ is replaced by β_b, and $\beta_c^{ir} + \beta_c^{s}$ is replaced by β_c. If the cylindrical wall is black, then $\beta_c^{s} = 0$ and $\beta_c^{ir} = \theta^4$.

Boundary Conditions at Exposed Tip; Severing of Conductive Contact at Base

As a supplement to the main concern of this investigation (i.e., the effect of radiation surface properties), two other aspects of the honeycomb absorber were examined. The first of these relates to the thermal boundary condition at the exposed tip of the cylindrical wall, that is, at $x = 0$. In the analysis described earlier in the report, it was assumed that the heat transfer at the exposed tip could be neglected, so that $d\theta/dX = 0$. Strictly speaking, this boundary condition corresponds to a perfectly reflecting tip surface

whose emittance is zero. Consideration will now be given to the other limiting case in which the exposed tip is a black surface.

An energy balance on a black tip surface yields

$$-k \frac{dT}{dx} = q^s - \sigma T^4 \tag{36}$$

or, in dimensionless terms,

$$\frac{d\theta}{dX} = \left(\frac{\sigma T_b^3 d}{k}\right)\left[\theta^4 - \left(\frac{q^s}{\sigma T_b^4}\right)\right] \tag{37}$$

which contains the new parameter $\sigma T_b^3 d/k$. Equation (37) serves as an alternative to equation (10) as the boundary condition at $X = 0$. Aside from this change in boundary condition, the governing equations remain unaltered from those presented earlier in the report. The results of solutions utilizing equation (37) will be given in the last part of the RESULTS AND DISCUSSION section.

The second supplemental study is concerned with the effect of severing conductive contact between the lower tip surface of the honeycomb (i.e., at $x = L$) and the base surface. The motivation for examining such a decoupling is the potential reduction in base surface heat loss that it affords. For the case in which the base surface is black and the lower tip surface is gray (emittance = ϵ_t), an energy balance at the lower tip gives

$$-k \frac{dT}{dx} = \epsilon_t \left(\sigma T^4 - \sigma T_b^4\right) \tag{38}$$

which becomes, after introduction of dimensionless variables,

$$\frac{d\theta}{dX} = \left(\frac{\epsilon_t \sigma T_b^3 d}{k}\right)(1 - \theta^4) \tag{39}$$

The boundary condition expressed by equation (39) serves as an alternative to that of equation (10) at $X = L/d$. The other governing equations remain unchanged. Results obtained by employing the boundary condition (39) will also be presented at the end of the RESULTS AND DISCUSSION section.

RESULTS AND DISCUSSION

Radiation Properties and Parameter Values

As a prelude to the presentation of the results, it is appropriate to set forth the radiation surface properties and the values of the other relevant parameters. A listing of the radiation surface properties is given in table I. As shown therein, a total of eight cases were considered, and the table indicates the values of α_b^s, ϵ_b^{ir}, α_c^s, and ϵ_c^{ir} for each case.

The first case, the black-surfaced cavity, provides continuity with the study reported in reference 5. Case 2 is a gray-walled cavity, with the value of ϵ being taken sufficiently different from one to ensure a clear indication of trends relative to case 1. The third case has a black base surface and a gray cylindrical wall. Cases 4, 5, and 6 are characterized by a selective base surface whose solar absorptance of 0.8 and infrared emittance of 0.2 represent reasonable objectives of a coating development program. These cases have cylindrical walls that are, respectively, black, gray, and selective. The selective base surface properties of cases 7 and 8 ($\alpha_b^s = 1.0$ and $\epsilon_b^{ir} = 0.2$), although not likely to be realized by present day technology, are included to permit a wide-ranging parametric study.

For the numerical solutions, the radiation-conduction parameter N, defined in equation (9), was assigned discrete values of 5, 10, 20, and 40. To provide perspective for this selection, it may be noted that for the conditions $T_b = 1144$ K (2060° R), d = 1.27 centimeters (0.5 in.), k = 0.208 W/(cm)(K) (1.0 Btu/(hr)(in.)($^\circ$R)), and t = 0.00254 centimeter (0.001 in.) (half thickness of actual honeycomb wall), the N parameter is approximately 26.

The bulk of the computations were performed for the depth-diameter ratio L/d = 5, with additional calculations for L/d = 7.5 and 10 to establish trends. The solar energy parameter $q^s/\sigma T_b^4$ was varied from a maximum value of 3 to a minimum value corresponding to $\eta = 0$. At a distance of 0.1 astronomical unit from the Sun and for $T_b = 1144$ K (2060° R), $q^s/\sigma T_b^4$ is approximately 1.44.

Absorber Efficiency

The efficiency characteristics of each of the eight cavity absorbers listed in table I have been determined in accordance with the analysis presented earlier in the report. This information has been plotted as curves of efficiency against the solar energy parameter $q^s/\sigma T_b^4$, each curve corresponding to a specific value of the radiation-conduction parameter N. The results for each of the cases of table I are given in a separate graph.

Before turning to this substantial and detailed body of information, it is worthwhile first to examine a more general set of results from which a number of trends and conclusions can be identified.

Comparisons of absorber efficiencies. - Figure 3 brings together the efficiency characteristics of all eight of the honeycomb absorbers listed in table I. The figure corresponds to $N = 20$ (a typical value of N) and to $L/d = 5$. The various curves are identified according to the numbers of the cases appearing in table I.

From an inspection of figure 3, it is seen that the efficiency increases monotonically with the solar energy parameter $q^s/\sigma T_b^4$. Thus, for example, for a fixed base temperature T_b, greater efficiencies are realized as the solar input q^s increases, that is, at positions nearer to the Sun. Efficiencies on the order of 80 percent and greater are generally attained for $q^s/\sigma T_b^4 > 1$ (except for the gray cavity, case 2). On the other hand, when $\eta = 0$, the solar radiation absorbed by the base is balanced out by the losses due to heat conduction to the honeycomb and radiation.

If the gray cavity (case 2) is excluded, then it is seen from figure 3 that the efficiency results for all of the other cavity absorbers fall within a rather narrow band; that is, the efficiency is relatively insensitive to the specifics of the radiation surface properties within the range considered. This desirable characteristic is especially in evidence in the range of higher efficiencies ($\eta \geq 0.5$), which is the range of greatest practical interest. The spread among the curves is somewhat greater at lower efficiencies, but if the nonselective base surfaces are excluded (cases 1, 2, and 3), then the remaining curves lie together in a tight band. These findings are based on the assumption of perfect alinement of the cavity axis with the direction of the incoming solar radiation.

The just-noted insensitivity of the efficiency to the radiation surface properties is, in itself, a finding of practical significance. In particular, if degradation of the cavity surfaces were to occur under space flight conditions, the absorption efficiency would not be seriously affected. Furthermore, it would appear unnecessary to strive to achieve a high degree of uniformity of the coatings applied to cavity surfaces. In contrast, as will be presently demonstrated, the efficiency of a plane plate absorber is drastically influenced by the specifics of the radiation surface properties.

Attention may now be redirected to figure 3 in order to highlight other aspects of the results presented therein. It may be seen that in the range of higher efficiencies (i.e., larger values of $q^s/\sigma T_b^4$), the efficiency is predominantly controlled by the base surface properties, with the properties of the cylindrical wall playing a secondary role. Indeed, high solar absorptance appears to be the critical factor. In this range, the curves for cases 4, 5, and 6 are nearly coincident, as are those for cases 7 and 8 and for cases 1 and 3. In the range of lower efficiencies (smaller values of $q^s/\sigma T_b^4$), better performance is attained for smaller values of the infrared emittance of the cylindrical wall.

To help provide perspective for the just-presented results, efficiencies for several plane plate absorbers have been computed and are plotted in figure 4. A plane plate

absorber is a plane surface whose normal is alined along the direction of the incident solar radiation. The efficiency is the ratio of the net rate of energy gain by the plane surface to the rate of arriving solar radiation. The solar absorptance α^s and the infrared emittance ϵ^{ir} appropriate to the cases considered are indicated in the figure. It is relevant to note that these α^s and ϵ^{ir} are identical to the radiation properties of the honeycomb base surfaces listed in table I.

Inspection of figure 4 shows that the efficiency of a plane plate absorber is strongly dependent on the radiation surface properties. In this respect, the results of figure 4 stand in sharp contrast to those of figure 3 for honeycomb absorbers. The comparison between the figures is particularly meaningful inasmuch as the honeycomb base surfaces and the plane plate absorbers have identical radiation properties. Clearly, if surface degradation were to occur in space flight, the plane plate absorber would be prone to a marked loss of efficiency.

A more detailed comparison between figures 3 and 4 indicates that the level of the efficiency achievable with a honeycomb absorber is higher than that achievable with a corresponding plane plate absorber. More direct comparisons of the two types of absorbers will be made in later figures (i.e., in figs. 5 to 15).

The efficiency results given in figure 3 for honeycomb absorbers correspond to a depth-diameter ratio $L/d = 5$. The effect of varying the L/d ratio is illustrated in figures 5, 6, and 7, respectively for cases 1, 4, and 6. Also included in each of these figures is a dashed line which represents the efficiency of a plane plate absorber having radiation properties identical to those of the corresponding honeycomb base surface.

Inspection of figures 5, 6, and 7 shows that larger values of L/d lead to increases in the level of the efficiency and also to a broadening of the range of $q^s/\sigma T_b^4$ in which $\eta \geq 0$. The most marked increases in efficiency occur when the efficiency is relatively low. In the range of higher efficiencies, only moderate gains in efficiency are realized with increasing cavity depth.

Figures 5, 6, and 7 also demonstrate the greater efficiencies attainable with the honeycomb absorber relative to those of a plane plate absorber. For the case of black surfaces (fig. 5), the differences in the efficiencies of the two types of absorbers are very large. Even for the realistic selective surfaces for which results are shown in figures 6 and 7, there are very substantial differences in the efficiencies of the honeycomb and plate absorbers. These comparisons provide motivation for giving consideration to the honeycomb absorber as a component of a solar power system.

Detailed presentation of efficiency results. - The efficiency characteristics of the honeycomb absorbers listed in table I are presented graphically in figures 8 to 15. The successive figures correspond to the successive cases appearing in the table. In each figure, the efficiency η is plotted as a function of the solar energy parameter $q^s/\sigma T_b^4$, with the radiation-conduction parameter N serving to identify the curves. The results presented in these figures are for a cavity depth-diameter ratio $L/d = 5$. Each figure

also contains a dashed curve corresponding to a plane plate absorber having radiation surface properties identical to those of the cavity base surface.

The figures show that the effects of increasing the N parameter are qualitatively similar to those resulting from increases in L/d, that is, the efficiency is higher and the range of $q^s/\sigma T_b^4$ in which $\eta \geq 0$ is broadened. The extent to which N influences the efficiency depends strongly on the magnitude of $q^s/\sigma T_b^4$. In particular, when $q^s/\sigma T_b^4 > 1$, the efficiency is virtually independent of N (at least within the range of N investigated herein). A practical corollary of this finding is that there is substantial freedom in choosing design parameters such as k, d, and t, provided that the system is to be operated in the range of larger values of $q^s/\sigma T_b^4$.

As $q^s/\sigma T_b^4$ decreases, the efficiency becomes more sensitive to N, the degree of the sensitivity depending on the radiation properties. From the figures, it is seen that for nonselective surfaces (cases 1, 2, and 3; figs. 8, 9, and 10), the spread of the curves with N is substantially less than that for the selective surfaces (cases 4 to 8; figs. 11 to 15).

Comparison of the results for honeycomb absorbers and plane plate absorbers indicate that the efficiencies of the former are generally higher. Only for cases 7 and 8 (figs. 14 and 15) is there overlap of the solid and dashed curves. For these cases, the radiation properties of the honeycomb base and of the plane plate (i.e., $\alpha^s = 1$, $\epsilon^{ir} = 0.2$) are, in themselves, highly favorable to the capture of solar radiation and to the minimization of heat losses. There is not a great deal of opportunity for improvement when such selective surfaces are employed. Therefore, if nondegrading selective surfaces of such quality could be made, the honeycomb absorber would show very little advantage in efficiency relative to the plane plate.

A careful inspection of figures 8 to 15 reveals that, in all cases where $\alpha_b^s < 1$, the efficiency curves tend to cross each other at the larger values of the solar energy parameter $q^s/\sigma T_b^4$. This behavior can be made plausible by examining distributions of the temperature along the cylindrical wall of the cavity. Figure 16 has been prepared for this purpose. Although the figure is specific to case 6, the temperature distributions shown therein are qualitatively representative of those for all cases for which $\alpha_b^s < 1$.

In figure 16, wall temperature distributions are plotted in the form $T_c(x)/T_b$ against x/L for parametric values of $q^s/\sigma T_b^4 = 3$, 1.4, and 0.6, with N = 20 and L/d = 5. Consider first the curve for $q^s/\sigma T_b^4 = 3$, which corresponds to the highest rate of arriving solar radiation. It is seen that for a substantial region of the cylindrical wall adjacent to the base surface, the temperature exceeds that of the base (i.e., $T_c/T_b > 1$). These elevated temperatures are caused by solar radiation which is incident on the cylindrical wall subsequent to being reflected by the base surface. One effect of such elevated surface temperatures is to increase the radiative heat loss from the cavity, which, in turn, tends to lower the efficiency.

The just-discussed elevation of the temperature of the cylindrical wall in the presence of large values of $q^s/\sigma T_b^4$ and $\alpha_b^s < 1$ is accentuated as the radiation-conduction parameter N increases. Correspondingly, at larger N, the radiative heat loss is greater. These greater losses cause the η curves for large N to fall below those for smaller N, as is evidenced in figures 9, 11, 12, and 13 in the range of large $q^s/\sigma T_b^4$.

As a final remark about figure 16, it may be observed that the temperature distribution curves for $q^s/\sigma T_b^4 = 1.4$ and 0.6 do not exhibit temperature elevations characterized by $T_c/T_b > 1$. The shapes of these curves are qualitatively representative of all temperature distributions corresponding to small and intermediate values of $q^s/\sigma T_b^4$ for all cases characterized by $\alpha_b^s < 1$. Furthermore, the temperature distributions for cases characterized by $\alpha_b^s = 1$ are also similar in shape to the lowermost curves of figure 16.

Effect of Boundary Conditions at x = 0 and x = L

All of the results presented thus far were based on the insulated tip boundary condition $d\theta/dX = 0$ at $X = 0$. The alternative boundary condition (37), which corresponds to a black tip surface, was employed in a limited number of solutions, and the corresponding efficiency results will now be discussed.

The additional solutions involving the alternative boundary condition were performed for the black-walled cavity (case 1), with $L/d = 5$, $N = 40$, $\sigma T_b^3\, d/k = 0.075$, and $q^s/\sigma T_b^4 = 1.4$ and 0.35. The efficiency was evaluated in accordance with equation (27), but now taking account of the role of the exposed tip of the cylindrical wall. If, as before, A_o represents the area of the cavity opening and if $A_t(=\pi\, dt)$ is the area of the exposed tip, then the efficiency for the case of a black tip surface can be expressed as

$$\eta = \frac{\left(q^s A_o - Q_o\right) + A_t\left[q^s - \sigma T^4(0)\right]}{q^s A_o + q^s A_t} \tag{40}$$

where Q_o is the radiant energy streaming from the cavity opening and $T(0)$ is the wall temperature at $x = 0$.

Numerical evaluation of equation (40) utilizing solutions corresponding to the aforementioned parameter values gives $\eta = 0.851$ and 0.425, respectively, for $q^s/\sigma T_b^4 = 1.4$ and 0.35. When compared with the η results for the insulated tip boundary condition (upper curve, fig. 8), near coincidence is attained. This finding suggests that particular account need not be taken of energy transfers at the exposed tip of the cylindrical wall.

The numerical exploration of the effect of severing conductive contact between the

lower tip surface of the honeycomb (i.e., at $x = L$) and the base surface was also performed for a black-walled cavity. The solutions involve the use of equation (39) as the boundary condition at $x = L$. Computations were carried out for $L/d = 5$, for N ranging from 5 to 40, and for $\epsilon_t \sigma T_b^3 \, d/k$ of 0.025, 0.050, and 0.075. The efficiencies evaluated from these solutions were found to be nearly identical to those for the case of conductive contact at the base (i.e., fig. 8). Thus, there appears to be no practical motivation for intentionally severing conductive contact between the honeycomb and the base.

SUMMARY AND CONCLUDING REMARKS

A two-band model for the radiation surface properties was used in formulating the integro-differential equations for simultaneous radiation and conduction in a cavity of a honeycomb absorber. Consideration was given to eight sets of radiation properties. The radiation properties of the base surface and of the cylindrical wall of the cavity were independently assigned. The radiation-conduction parameter N was varied from 5 to 40, while the depth-diameter ratio L/d covered the range from 5 to 10. Values of the solar energy parameter $q^s/\sigma T_b^4$, which played the role of the independent variable in the presentation of results, ranged from a maximum of 3 to a minimum corresponding to zero net absorption of energy. In the analysis, it was assumed that the incoming solar radiation is alined with the axis of the cavity absorber.

The performance of the honeycomb absorber was characterized by an efficiency which is the ratio of the net energy gain of the base surface to the arriving solar radiation. An extensive graphical presentation of efficiency results was made for the just-mentioned parameter ranges. This information should be applicable to design. Efficiencies were also computed for plane plate absorbers having radiation properties identical to those of the honeycomb base surfaces.

The efficiencies of the honeycomb absorbers investigated herein were found to be relatively insensitive to the specifics of the radiation surface properties, particularly in the range of higher efficiencies. This behavior stands in contrast to that of the plane plate absorber, which is highly sensitive to the surface properties. The honeycomb absorber thus appears to be attractive for applications where surface degradation is likely to occur. Furthermore, for realistic surface properties, the efficiency of a honeycomb absorber is substantially greater than that of a plane plate absorber assuming that the aforementioned perfect alinement can be achieved.

Increasing cavity depth tends to increase the absorber efficiency, particularly in the range where the efficiency is low. At higher efficiencies, the performance of the honeycomb absorber is relatively insensitive to the depth-diameter ratio. The effects of in-

creasing the radiation-conduction parameter N are qualitatively similar to those of increasing cavity depth. The relative insensitivity of honeycomb absorber performance to both L/d and N in the range of higher efficiencies makes for considerable latitude in the choice of thermal and geometrical design parameters.

Exploratory computations showed that the efficiency results are essentially unaffected by a change in the boundary condition at the exposed tip and by severing conductive contact between the honeycomb and the base surface.

Lewis Research Center,
National Aeronautics and Space Administration,
Cleveland, Ohio, January 27, 1971,
120-33.

APPENDIX A

SYMBOLS

A	area
B	radiosity
d	cavity diameter
F	angle factor
H	incident radiation per unit time and area
k	thermal conductivity
L	cavity depth
N	radiation-conduction parameter
Q	rate of energy transfer
q^s	arriving solar radiation per unit time and area
T	absolute temperature
t	thickness of cylindrical wall
X	dimensionless axial coordinate
x	axial coordinate
α	absorptance
β	dimensionless radiosity
ϵ	emittance
$\overline{\epsilon}$	apparent emittance
ζ	dimensionless radial coordinate
η	efficiency
θ	dimensionless temperature
ξ	dummy integration variable
ρ	reflectance
σ	Stefan-Boltzmann constant

Subscripts:

b	base surface
c	cylindrical wall
cond	conduction
o	cavity opening
rad	radiation
t	tip

Superscripts:

ir	infrared range
s	solar range

APPENDIX B

ANGLE FACTORS

The expressions for the angle factors that were employed in the ANALYSIS section are given in this appendix. These expressions are identical to those of reference 5 and have also appeared elsewhere in the literature.

$$dF_{X-\xi} = \left\{ 1 - \frac{|X - \xi| \left[2(X - \xi)^2 + 3 \right]}{2\left[(X - \xi)^2 + 1 \right]^{3/2}} \right\} d\xi \tag{B1}$$

$$F_{X-b} = \frac{1 + 2\left(\frac{L}{d} - X\right)^2}{2\left[\left(\frac{L}{d} - X\right)^2 + 1\right]^{1/2}} - \left(\frac{L}{d} - X\right) \tag{B2}$$

$$F_{b-o} = 1 + 2\left(\frac{L}{d}\right)^2 - 2\left(\frac{L}{d}\right)\sqrt{\left(\frac{L}{d}\right)^2 + 1} \tag{B3}$$

The angle factor $F_{\xi-b}$ is obtained from equation (B2) by replacing X with ξ. Also, $F_{\xi-o}$ follows by substituting ξ in place of $(L/d) - X$ on the right side of equation (B2).

APPENDIX C

EFFECT OF BASE SURFACE RADIOSITY VARIATION

In the development of the governing equations as described in the ANALYSIS section, the base surface radiosity was taken to be spatially uniform. The effect of spatial variations of the base surface radiosity will now be investigated.

The subsequent analysis and associated numerical solutions are carried out for the gray-walled cavity. The energy balance differential equation (26) and the boundary conditions (10) continue to apply, but equation (25) is replaced by a pair of coupled integral equations. The first of these integral equations is derived by evaluating the radiosity equation (11) (in which the superscript ir is now omitted) at a typical location x on the cylindrical wall. The evaluation parallels that previously described in connection with equation (15), but with account taken of the spatial dependence of the base surface radiosity. The end result of the derivation is

$$\beta_c(X) = \epsilon\theta^4(X) + (1 - \epsilon)\left[\int_{\xi=0}^{L/d} \beta_c(\xi)dF_{X-\xi} + \int_{\zeta=0}^{1} \beta_b(\zeta)dF_{X-\zeta}\right] \tag{C1}$$

where ζ is a dimensionless radial coordinate which is zero at the center of the base surface and unity at the rim of the base surface.

The second integral equation is derived by evaluating the radiosity equation (16) (with ir deleted) at a typical radial position on the base surface, with the result

$$\beta_b(\zeta) = \epsilon + (1 - \epsilon)\left[\int_{\xi=0}^{L/d} \beta_c(\xi)dF_{\zeta-\xi} + \frac{q^s}{\sigma T_b^4}\right] \tag{C2}$$

The angle factor $dF_{X-\xi}$ is already given in appendix B, and $dF_{X-\zeta}$ and $dF_{\zeta-\xi}$ may be expressed as

$$\left.\begin{aligned} dF_{X-\zeta} &= \Omega(X, \zeta)\zeta\, d\zeta \\ dF_{\zeta-\xi} &= 2\Omega(\xi, \zeta)d\xi \end{aligned}\right\} \tag{C3}$$

where

$$\Omega(\lambda,\zeta) = \frac{4\left(\frac{L}{d}-\lambda\right)\left[4\left(\frac{L}{d}-\lambda\right)^2+1-\zeta^2\right]}{\left\{\left[4\left(\frac{L}{d}-\lambda\right)^2+1+\zeta^2\right]^2-4\zeta^2\right\}^{3/2}}$$

When the just-derived equations (C1) and (C2) are taken together with the differential equation (26) and boundary conditions (10), there emerges an integro-differential system for the three unknowns $\theta(X)$, $\beta_c(X)$, and $\beta_b(\zeta)$. By utilizing the numerical solutions of this system, the absorber efficiency can be evaluated from equation (31) wherein the apparent emittance $\bar{\epsilon}$ is now expressed by

$$\bar{\epsilon} = 2\int_{\zeta=0}^{1}\beta_b(\zeta)F_{\zeta-o}\,\zeta\,d\zeta + 4\int_{\xi=0}^{L/d}\beta_c(\xi)F_{\xi-o}\,d\xi \tag{C4}$$

in which

$$2F_{\zeta-o} = 1 - \frac{4\left(\frac{L}{d}\right)^2-1+\zeta^2}{\left\{\left[4\left(\frac{L}{d}\right)^2+1+\zeta^2\right]^2-4\zeta^2\right\}^{1/2}} \tag{C5}$$

and $F_{\xi-o}$ is given in appendix B.

Numerical solutions of the just-formulated governing equations were carried out for $\epsilon = 0.5$, $L/D = 5$, $N = 20$, and for $q^s/\sigma T_b^4$ ranging from 3 to a minimum value at which $\eta = 0$. The efficiencies evaluated from these solutions are plotted in figure 17, where they are compared with a corresponding set of results based on the assumption of uniform base surface radiosity. From an inspection of the figure, it is seen that the two curves appearing therein are nearly coincident, with the largest deviations being encountered in the range of low efficiencies.

In light of figure 17, the uncertainty introduced by assuming uniform base surface radiosity appears to be entirely tolerable, especially in view of the reduction in computation time that is thereby realized.

APPENDIX D

NUMERICAL SOLUTION METHOD

The method employed to obtain solutions of the integro-differential systems encountered earlier in the report will now be outlined. The solutions were carried out numerically with the aid of an IBM 7094 digital computer. In essence, the governing integral and differential equations were reduced to finite-difference form and, after interim linearization, the resulting algebraic system was solved by means of a linear equation solver. Inasmuch as the method of approach was identical for all of the equation systems treated herein, it will be sufficient to discuss only the gray-walled cavity, the equations for which (i.e., eqs. (25), (26), and (10)) are somewhat simpler than those for the two-band model.

Attention may first be turned to the formation of the difference equations. The derivatives $d^2\theta/dX^2$ and $d\theta/dX$, respectively, appearing in equations (26) and (10), were discretized in a straightforward manner via central differences. On the other hand, the discretization of the integral terms in equation (25) requires greater care. In particular, consider the first integral on the right side. The angle factor $dF_{X-\xi}$, expressed by equation (B1), undergoes a very rapid variation in the neighborhood of $X = \xi$. Consequently, discretization by standard methods such as the trapezoidal rule or Simpson's rule would require that an excessively large number of mesh points be employed in order to achieve acceptable accuracy.

To circumvent this difficulty, the following approach was employed to derive an algebraic form of the integral. To begin, let

$$I_j(X) = \int_{\xi_j}^{\xi_{j+1}} \beta(\xi) dF_{X-\xi} \tag{D1}$$

so that

$$\int_{\xi=0}^{L/d} \beta(\xi) dF_{X-\xi} = \sum_{j=1}^{M-1} I_j(X) \tag{D2}$$

where $\xi_1 = 0$, $\xi_M = L/d$, and $\xi_{j+1} - \xi_j = \Delta\xi = (L/d)/(M - 1)$. In any interval $\xi_j \le \xi \le \xi_{j+1}$, $\beta(\xi)$ was represented as a straight line

$$\beta(\xi) = C_j + D_j \xi \tag{D3}$$

in which

$$C_j \, \Delta\xi = \beta_j \xi_{j+1} - \beta_{j+1} \xi_j$$

$$D_j \, \Delta\xi = \beta_{j+1} - \beta_j$$

The linear relation (D3) was then substituted into equation (D1) along with the angle factor from equation (B1). The resulting integration was carried out without approximation and in closed form, yielding an algebraic expression which can be written schematically as

$$I_j(X) = G_j \beta_j + K_j \beta_{j+1} \tag{D4}$$

The G_j and K_j are lengthy expressions involving X, ξ_j, ξ_{j+1}, and $\Delta\xi$. Finally, substitution of equation (D4) into equation (D2) yields a representation of the integral as a linear sum of the discrete set of unknowns $\beta_1, \beta_2, \ldots, \beta_M$.

The just-described procedure was also employed to discretize the second integral appearing in equation (25). Thus, in this way, the governing equations (25), (26), and (10) were recast in finite-difference form.

The algebraic equations thus obtained are nonlinear owing to the terms involving θ^4 and θ in equations (25) and (26). To facilitate the numerical solution, an interim linearization was made, the form of which is suggested by a Taylor's series expansion. Thus, θ^4 is written as

$$\theta^4 = 4\theta\hat{\theta}^3 - 3\hat{\theta}^4 \tag{D5}$$

Clearly, equation (D5) reduces to an indentity when $\hat{\theta} = \theta$. For the present, $\hat{\theta}$ may be regarded as a known function of X. Equation (D5) is incorporated into the discretized forms of equations (25) and (26).

It thus remains to solve a set of linear algebraic equations for the discrete set of unknowns θ_j and β_j. For this purpose, a modified Gauss-Seidel method was employed, with all computations being performed in double-precision arithmetic. The linear equation solver was employed in an iterative manner in order to ultimately satisfy the condition $\hat{\theta} = \theta$.

To initiate the calculations, $\hat{\theta}$ was taken as a straight line between the values $\theta(L/d) = 1$ and $\theta(0) = 0.7$. With this $\hat{\theta}$ as input, the linear equation system was solved for the β_j and θ_j. Then, these output values of θ_j were used as the $\hat{\theta}$ input for a

second solution of the set of linear equations. This procedure of using output values of θ as input values of $\hat{\theta}$ for a subsequent solution was continued until the following condition was satisfied at all points:

$$\left|1 - \frac{\hat{\theta}}{\theta}\right| < 0.000001 \tag{D6}$$

Typically, equation (D6) was fulfilled within four or five iterations.

In the numerical solutions, 110 equally spaced mesh points were used along the cylindrical wall. For the investigation described in appendix C, 110 mesh points were also used along the radial coordinate of the base surface.

REFERENCES

1. Francia, Giovanni: A New Collector of Solar Radiant Energy: Theory and Experimental Verification-Calculation of the Efficiencies. Paper 594B, SAE, Oct. 1962.
2. Hollands, K. G. T.: Honeycomb Devices in Flat-Plate Solar Collectors. Solar Energy, vol. 9, no. 3, July-Sept. 1965, pp. 159-164.
3. Perrot, M.; Gallet, P.; Peri, G.; Desautel, J.; and Touchais, M.: Antiradiant Cellular Structures and Their Industrial Applications. Solar Energy, vol. 11, no. 1, Jan.-Mar. 1967, pp. 34-40.
4. Pellette, P.; Cobble, M.; and Smith, P.: Honeycomb Thermal Trap. Solar Energy, vol. 12, no. 2, Dec. 1968, pp. 263-265.
5. Bifano, William J.: Preliminary Analysis of a Titanium Alloy Honeycomb Solar Absorber Having Blackened Walls. NASA TN D-4727, 1968.

TABLE I. - RADIATION SURFACE PROPERTIES

Case	Solar absorptance of base surface, α_b^s	Infrared emittance of base surface, ϵ_b^{ir}	Solar absorptance of cylindrical wall, α_c^s	Infrared emittance of cylindrical wall, ϵ_c^{ir}
1	1.0	1.0	1.0	1.0
2	.5	.5	.5	.5
3	1.0	1.0	.5	.5
4	.8	.2	1.0	1.0
5	.8	.2	.5	.5
6	.8	.2	.8	.2
7	1.0	.2	1.0	1.0
8	1.0	.2	.5	.5

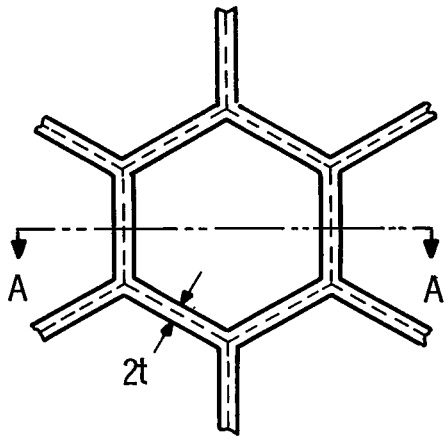

(a) Full face view.

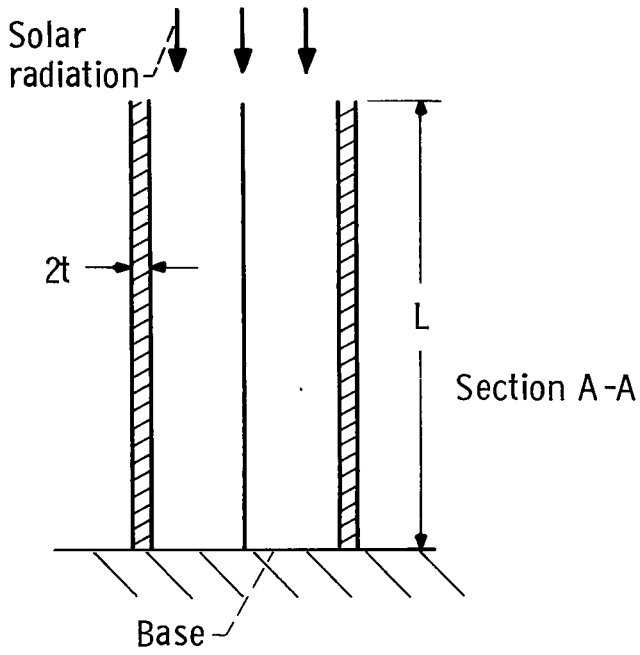

(b) Sectional view through A-A.

Figure 1. - Typical element of honeycomb.

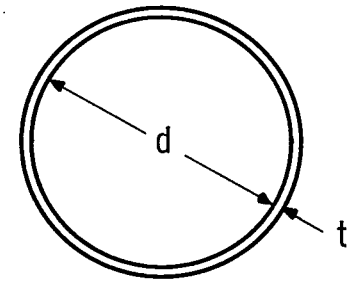

(a) Top view.

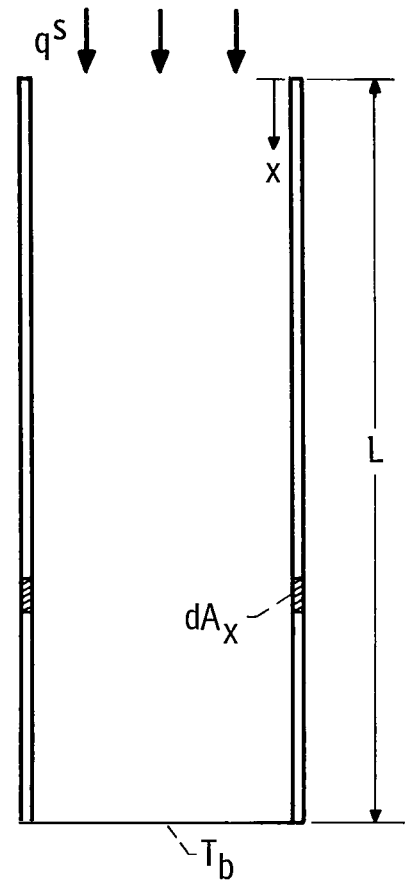

(b) Sectional view.

Figure 2. - Circular cylindrical cavity.

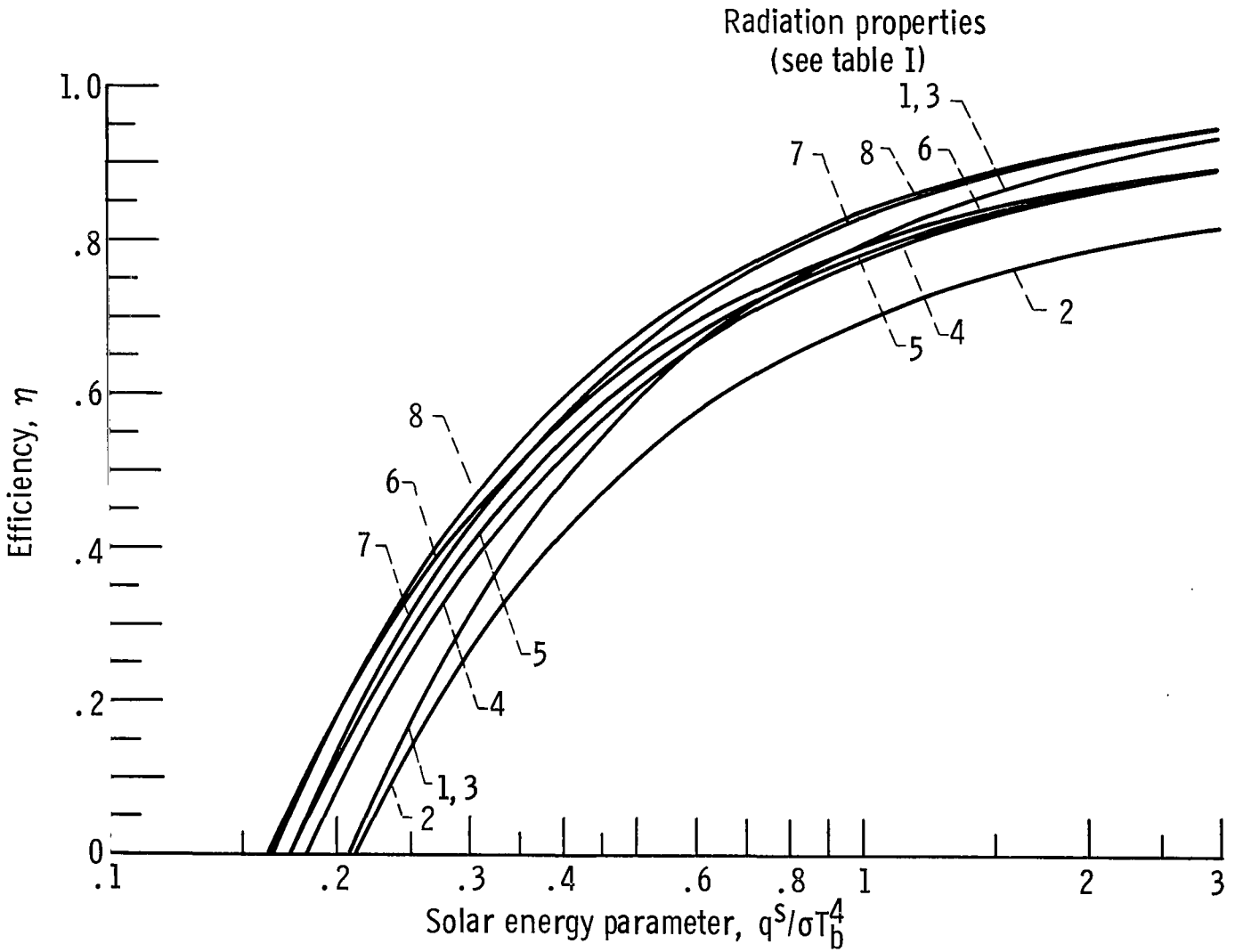

Figure 3. - Comparison of efficiencies of various honeycomb absorbers. Radiation-conduction parameter N = 20; depth-diameter ratio, L/d = 5.

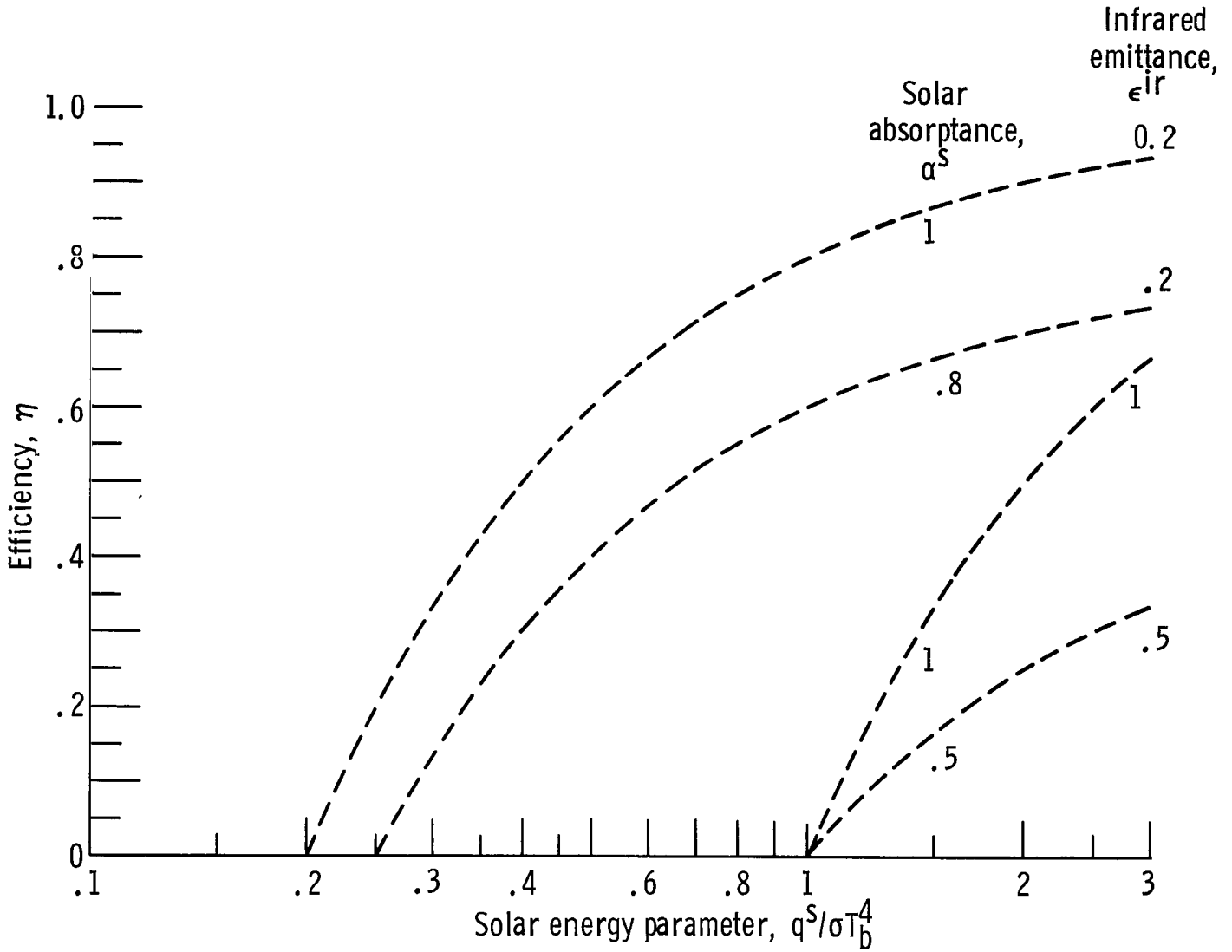

Figure 4. - Efficiencies of plane plate absorbers.

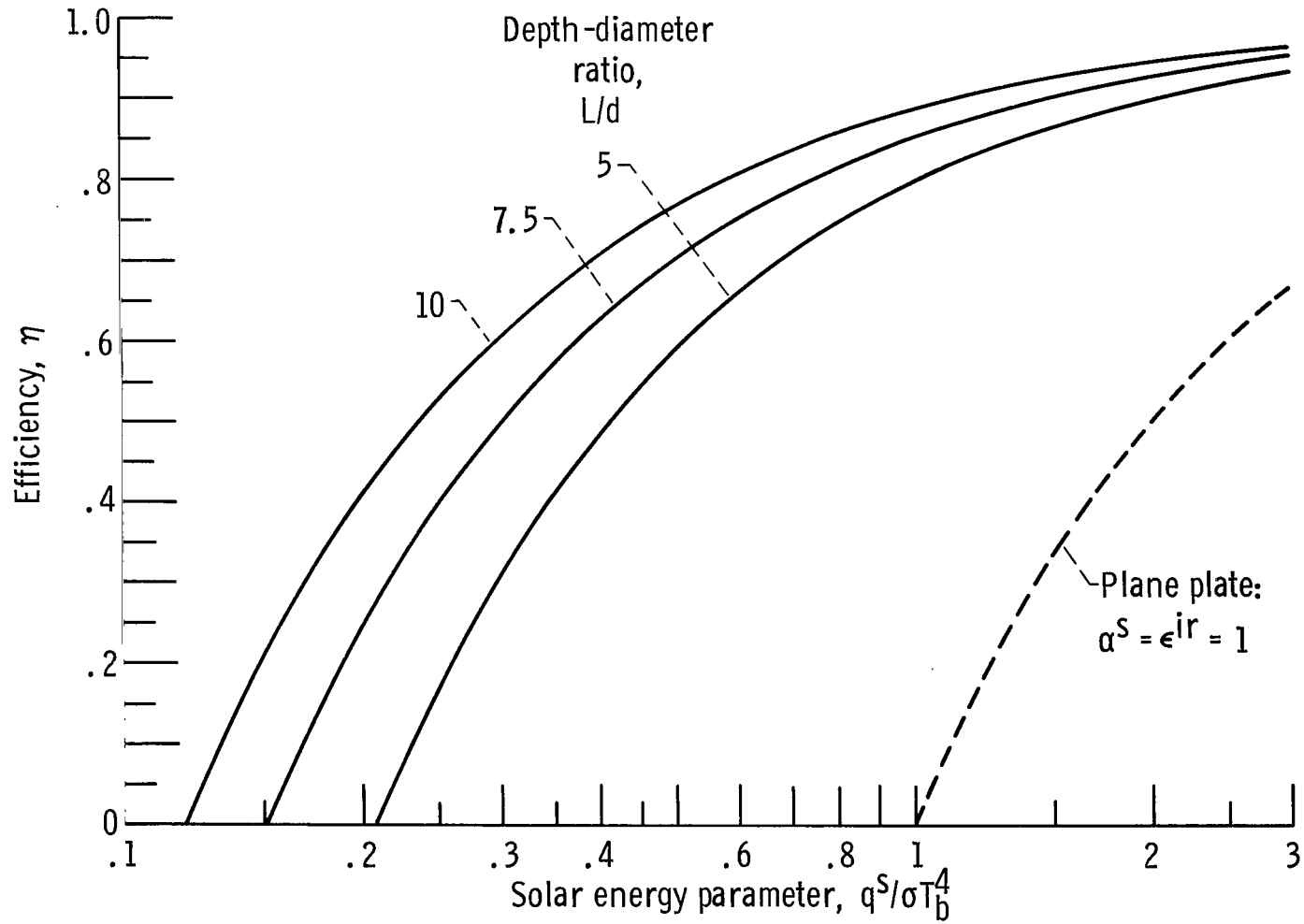

Figure 5. - Effect of cavity depth-diameter ratio on absorber efficiency. Case 1: $\alpha_b^s = \epsilon_b^{ir} = 1$; $\alpha_c^s = \epsilon_c^{ir} = 1$. Radiation-conduction parameter N = 20.

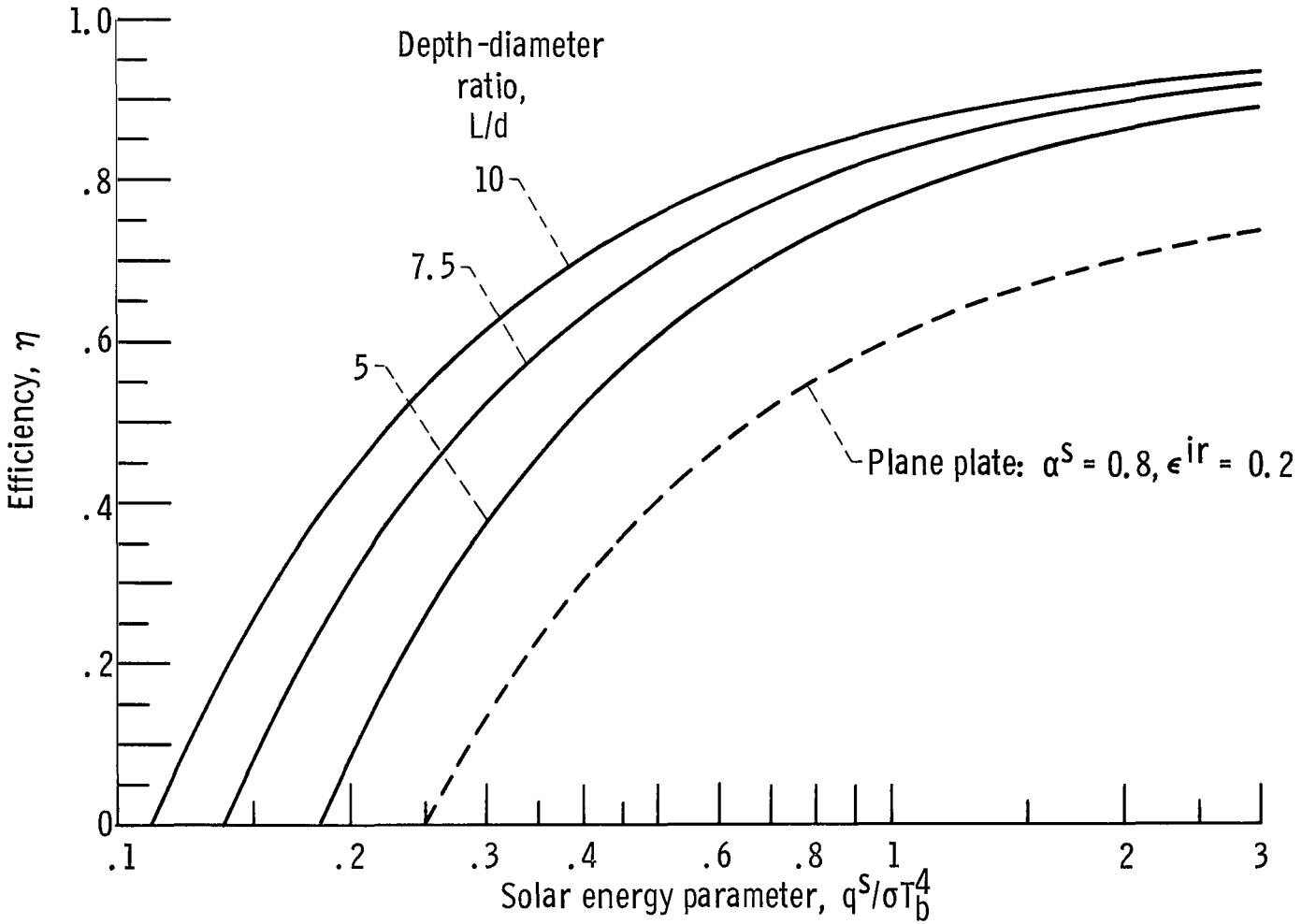

Figure 6. - Effect of cavity depth-diameter ratio on absorber efficiency. Case 4: $\alpha_b^s = 0.8$; $\epsilon_b^{ir} = 0.2$; $\alpha_c^s = \epsilon_c^{ir} = 1$. Radiation-conduction parameter N = 20.

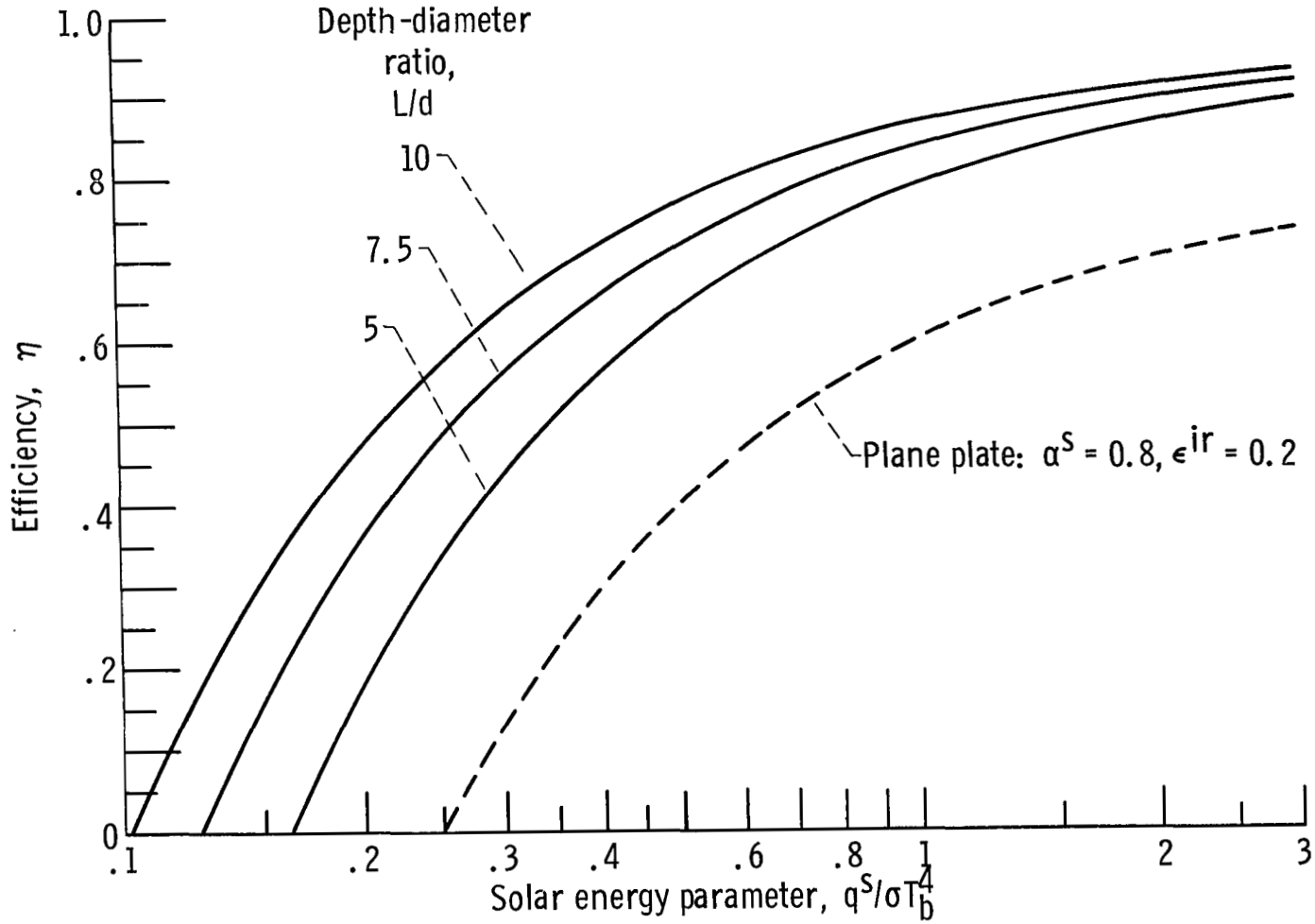

Figure 7. - Effect of cavity depth-diameter ratio on absorber efficiency. Case 6: $\alpha_b^s = 0.8$, $\epsilon_b^{ir} = 0.2$; $\alpha_c^s = 0.8$, $\epsilon_c^{ir} = 0.2$. Radiation-conduction parameter N = 20.

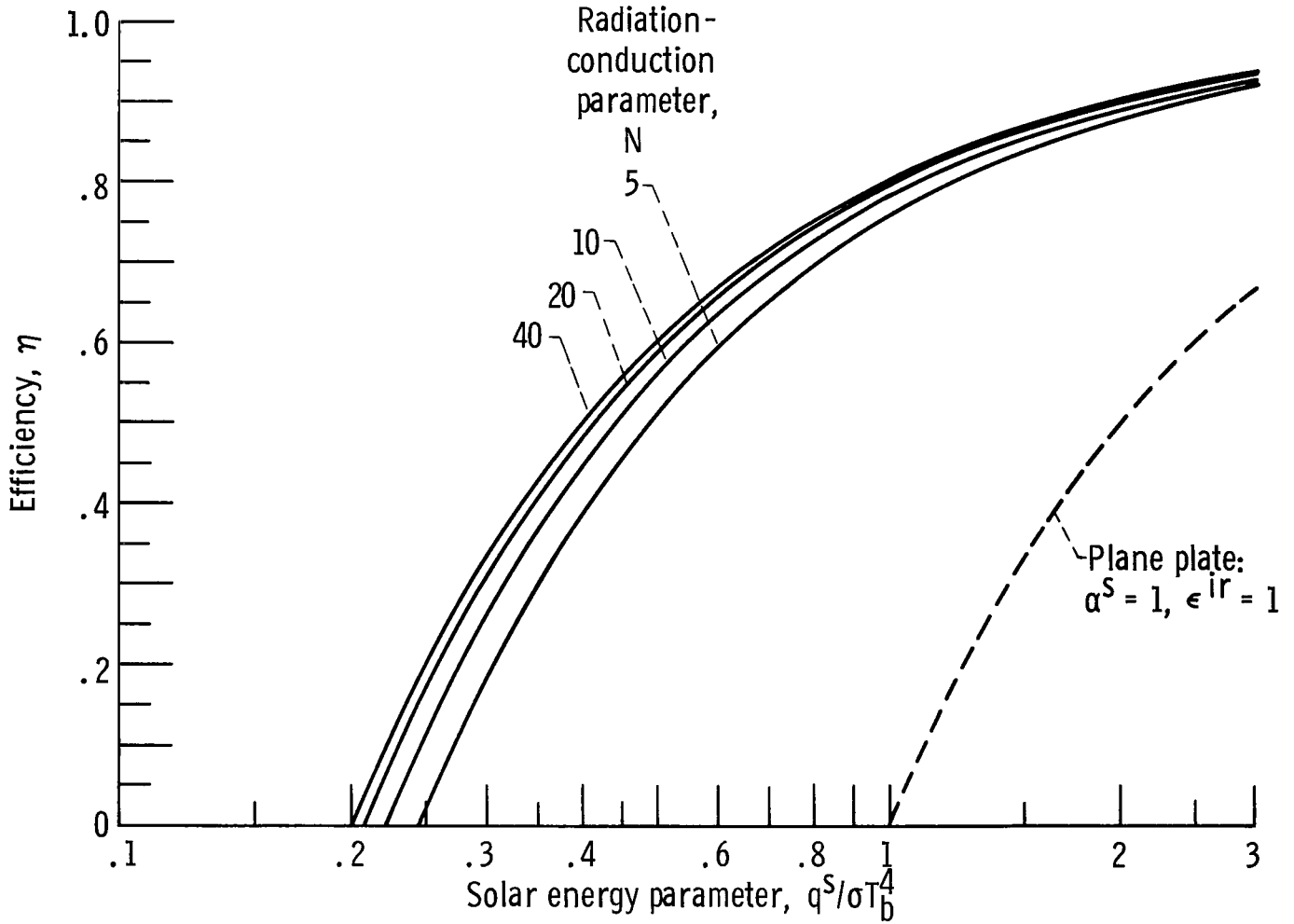

Figure 8. - Honeycomb absorber efficiency results. Case 1: $\alpha_b^s = \epsilon_b^{ir} = 1$; $\alpha_c^s = \epsilon_c^{ir} = 1$. Depth-diameter ratio L/d = 5.

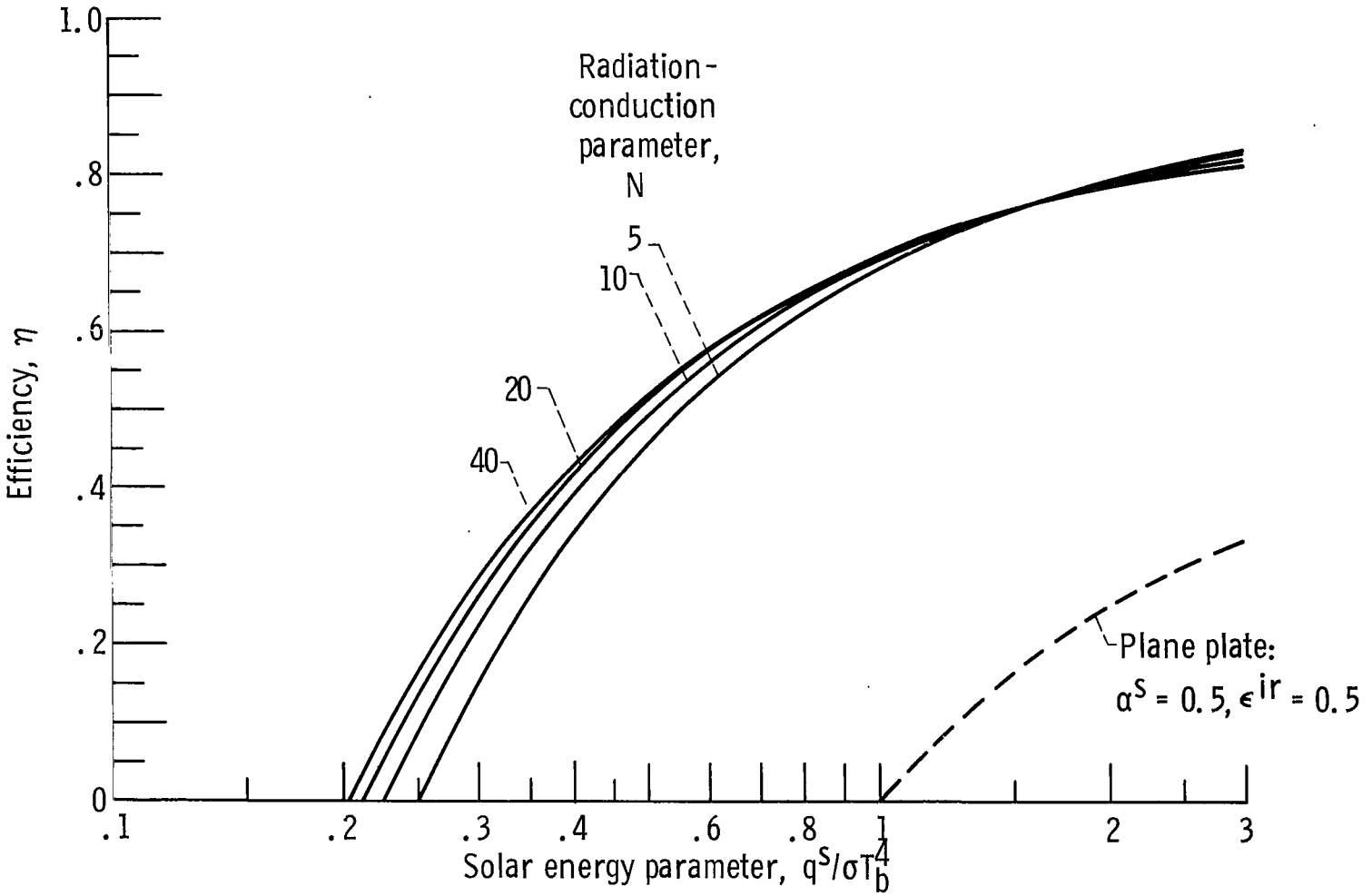

Figure 9. - Honeycomb absorber efficiency results. Case 2: $\alpha_b^S = \epsilon_b^{ir} = 0.5$; $\alpha_c^S = \epsilon_c^{ir} = 0.5$. Depth-diameter ratio L/d = 5.

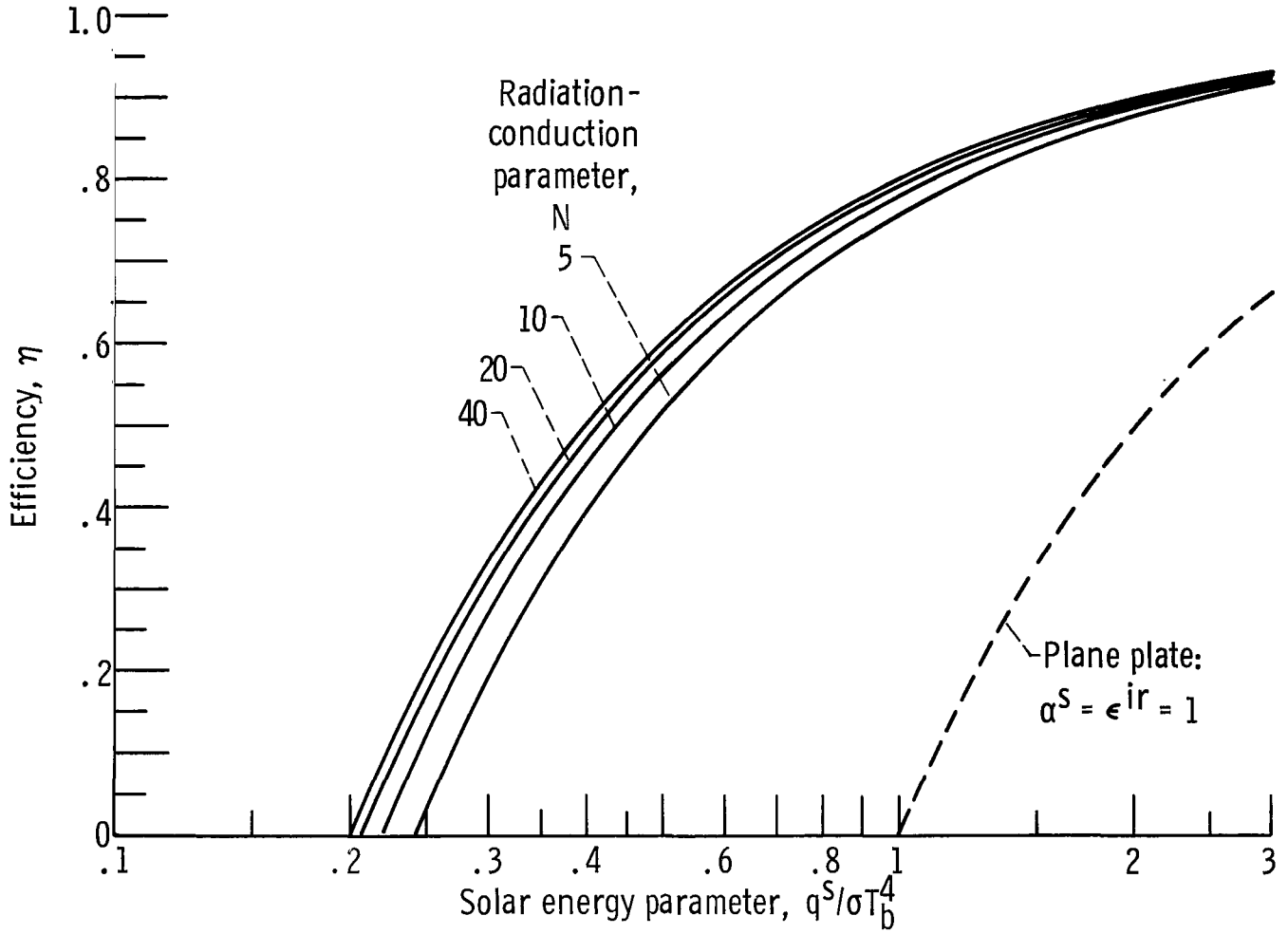

Figure 10. - Honeycomb absorber efficiency results. Case 3: $\alpha_b^s = \epsilon_b^{ir} = 1$; $\alpha_c^s = \epsilon_c^{ir} = 0.5$. Depth-diameter ratio L/d = 5.

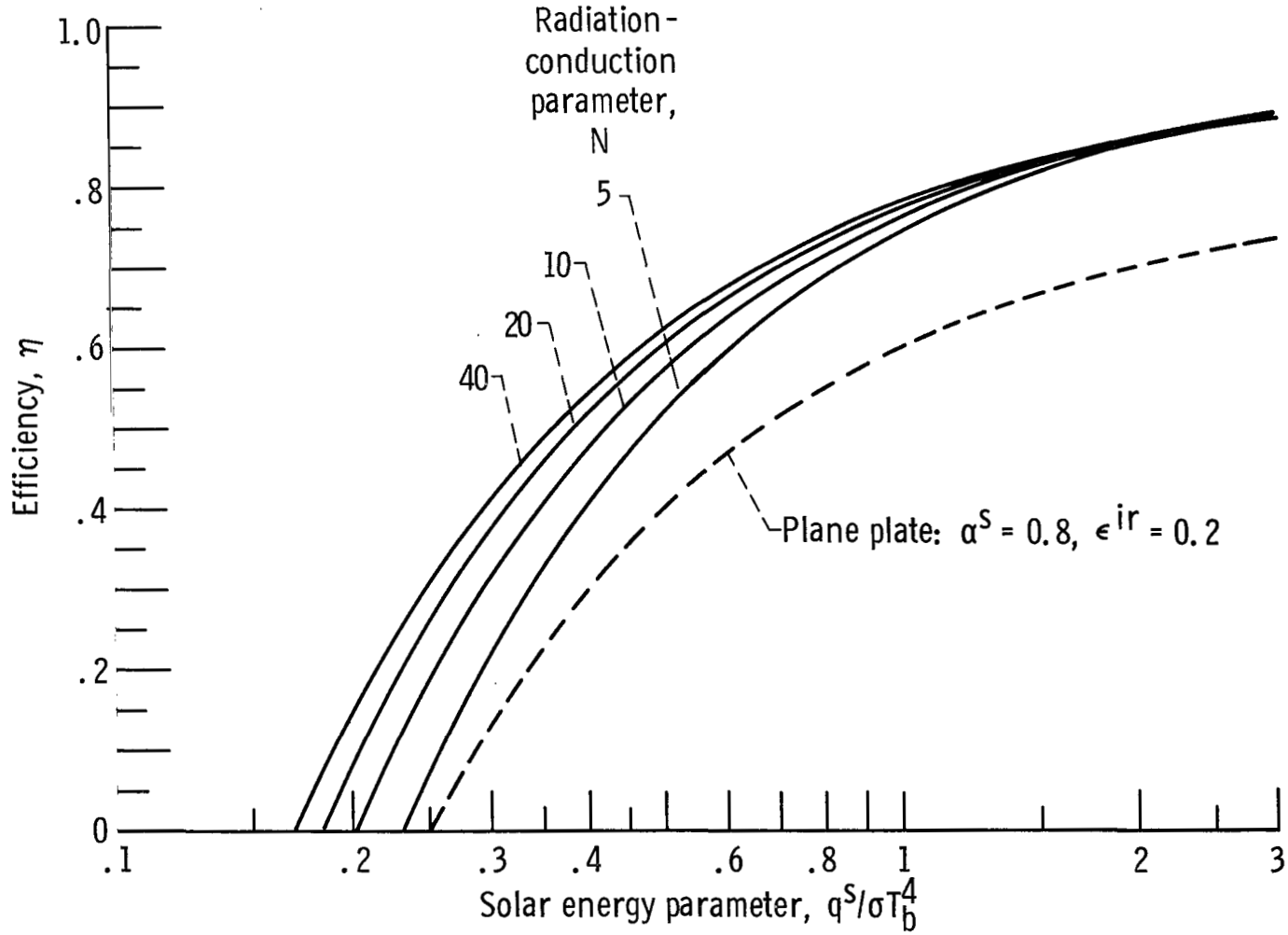

Figure 11. - Honeycomb absorber efficiency results. Case 4: $\alpha_b^s = 0.8$, $\epsilon_b^{ir} = 0.2$; $\alpha_c^s = \epsilon_c^{ir} = 1$. Depth-diameter ratio L/d = 5.

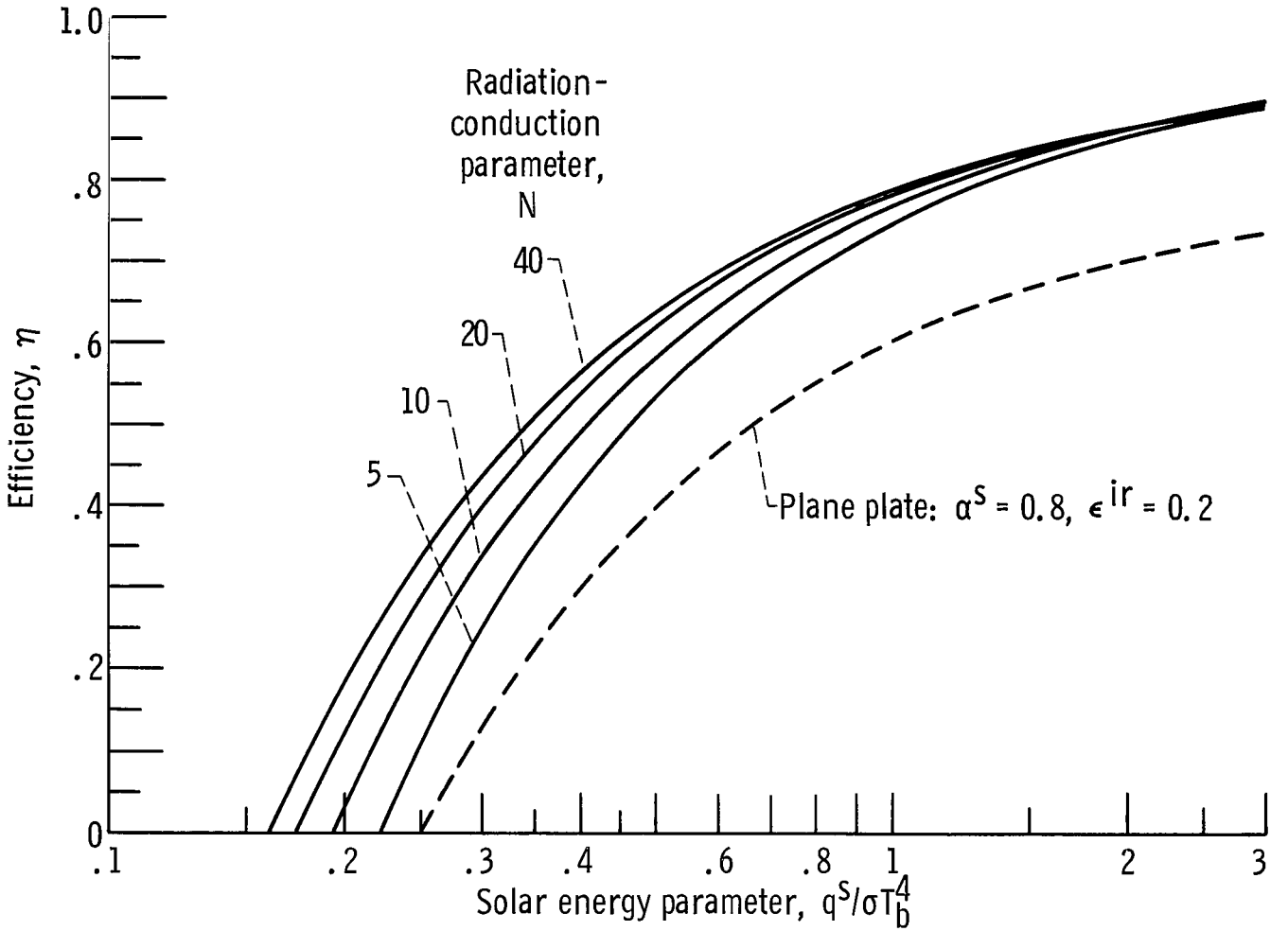

Figure 12. - Honeycomb absorber efficiency results. Case 5: $\alpha_b^s = 0.8$, $\epsilon_b^{ir} = 0.2$; $\alpha_c^s = \epsilon_c^{ir} = 0.5$. Depth-diameter ratio L/d = 5.

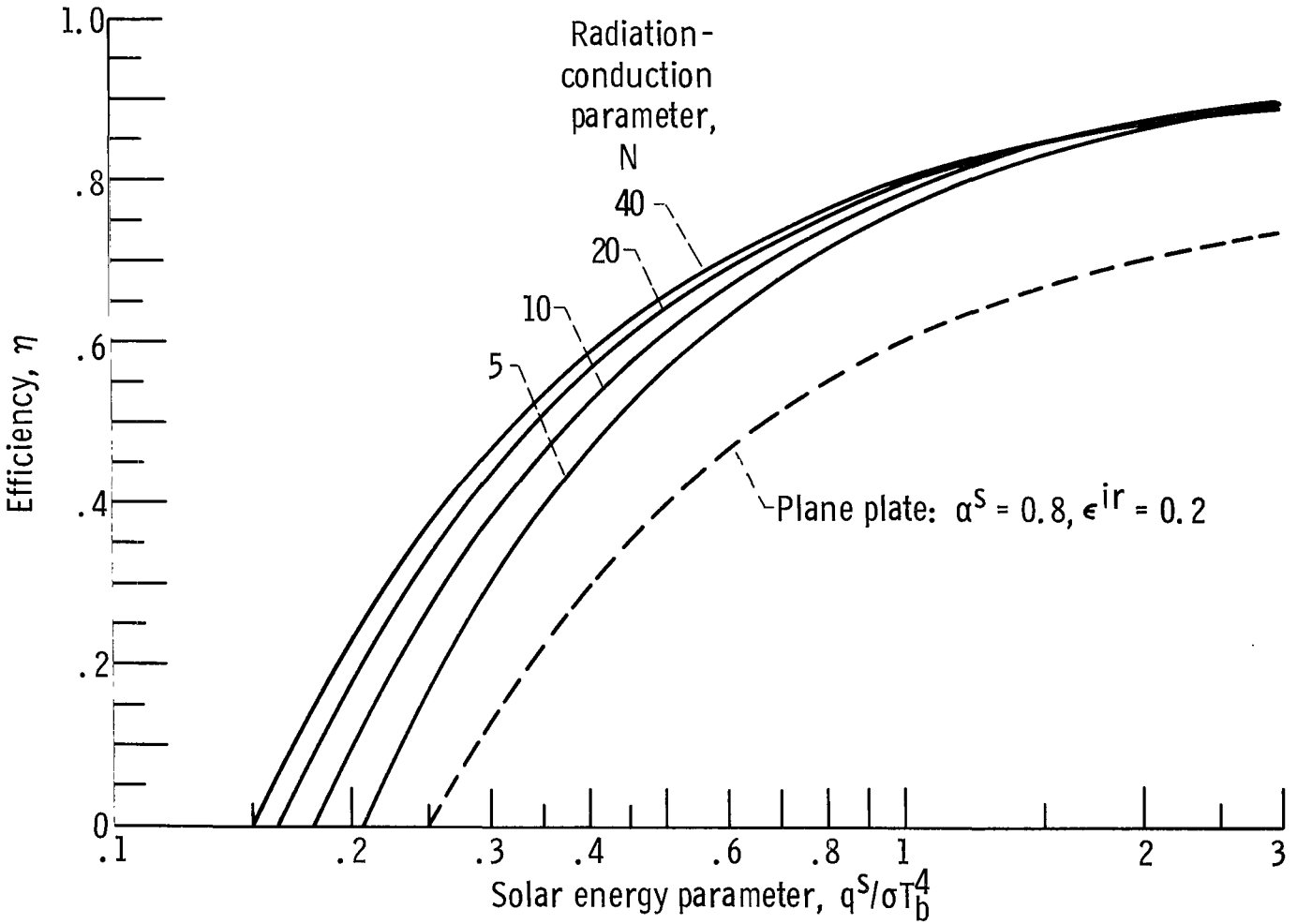

Figure 13. - Honeycomb absorber efficiency results. Case 6: $\alpha_b^s = 0.8$, $\epsilon_b^{ir} = 0.2$; $\alpha_c^s = 0.8$, $\epsilon_c^{ir} = 0.2$.

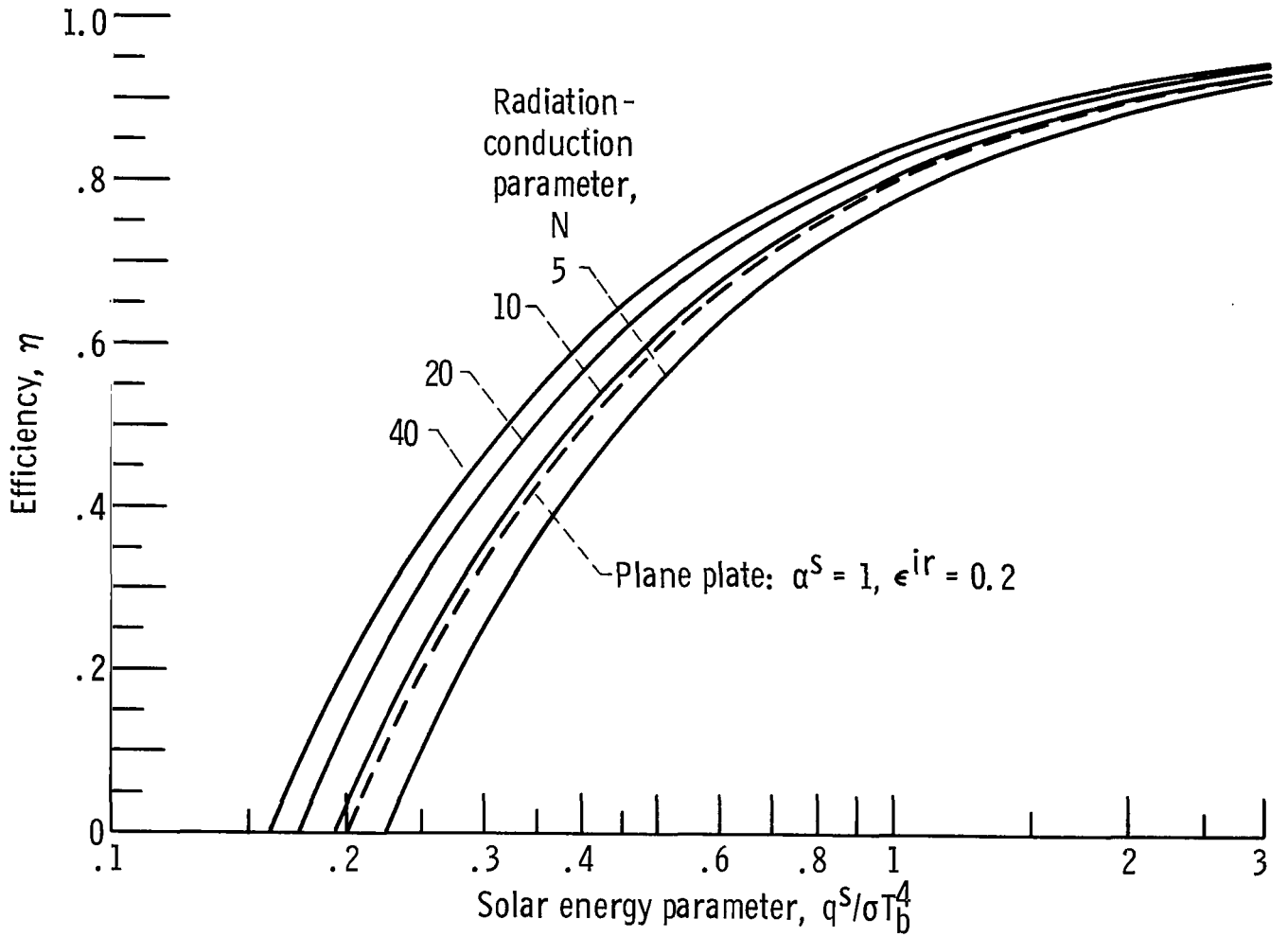

Figure 14. - Honeycomb absorber efficiency results. Case 7: $\alpha_b^s = 1$, $\epsilon_b^{ir} = 0.2$; $\alpha_c^s = \epsilon_c^{ir} = 1$. Depth-diameter ratio L/d = 5.

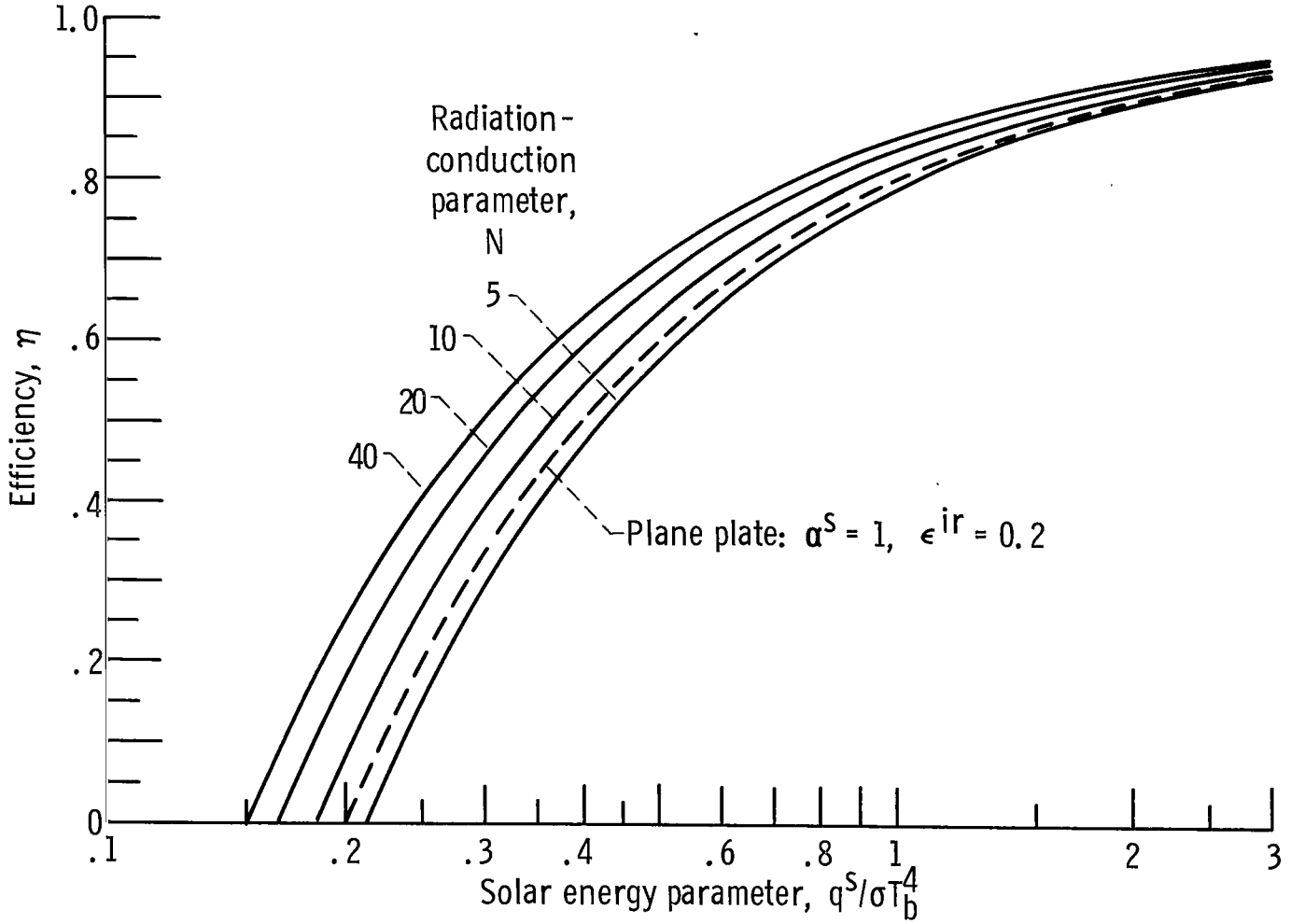

Figure 15. - Honeycomb absorber efficiency results. Case 8: $\alpha_b^S = 1$, $\epsilon_b^{ir} = 0.2$; $\alpha_c^S = \epsilon_c^{ir} = 0.5$. Depth-diameter ratio L/d = 5.

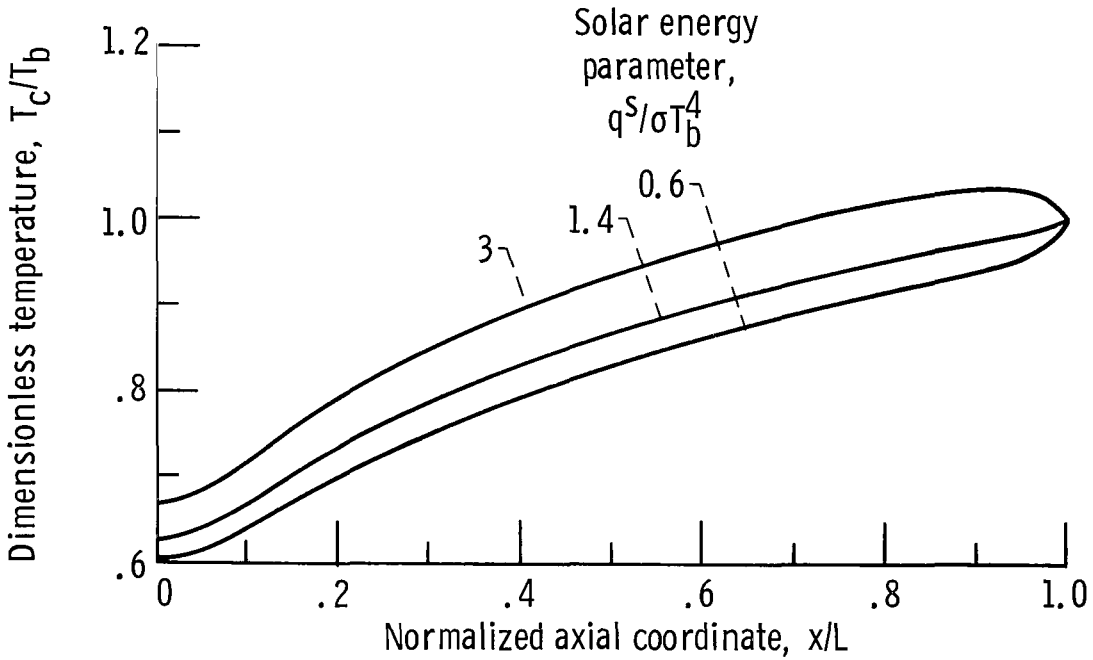

Figure 16. - Representative wall temperature distributions. Case 6: $\alpha_b^S = 0.8$, $\epsilon_b^{Ir} = 0.2$; $\alpha_c^S = 0.8$, $\epsilon_c^{Ir} = 0.2$. Radiation-conduction parameter N = 20; depth-diameter ratio L/d = 5.

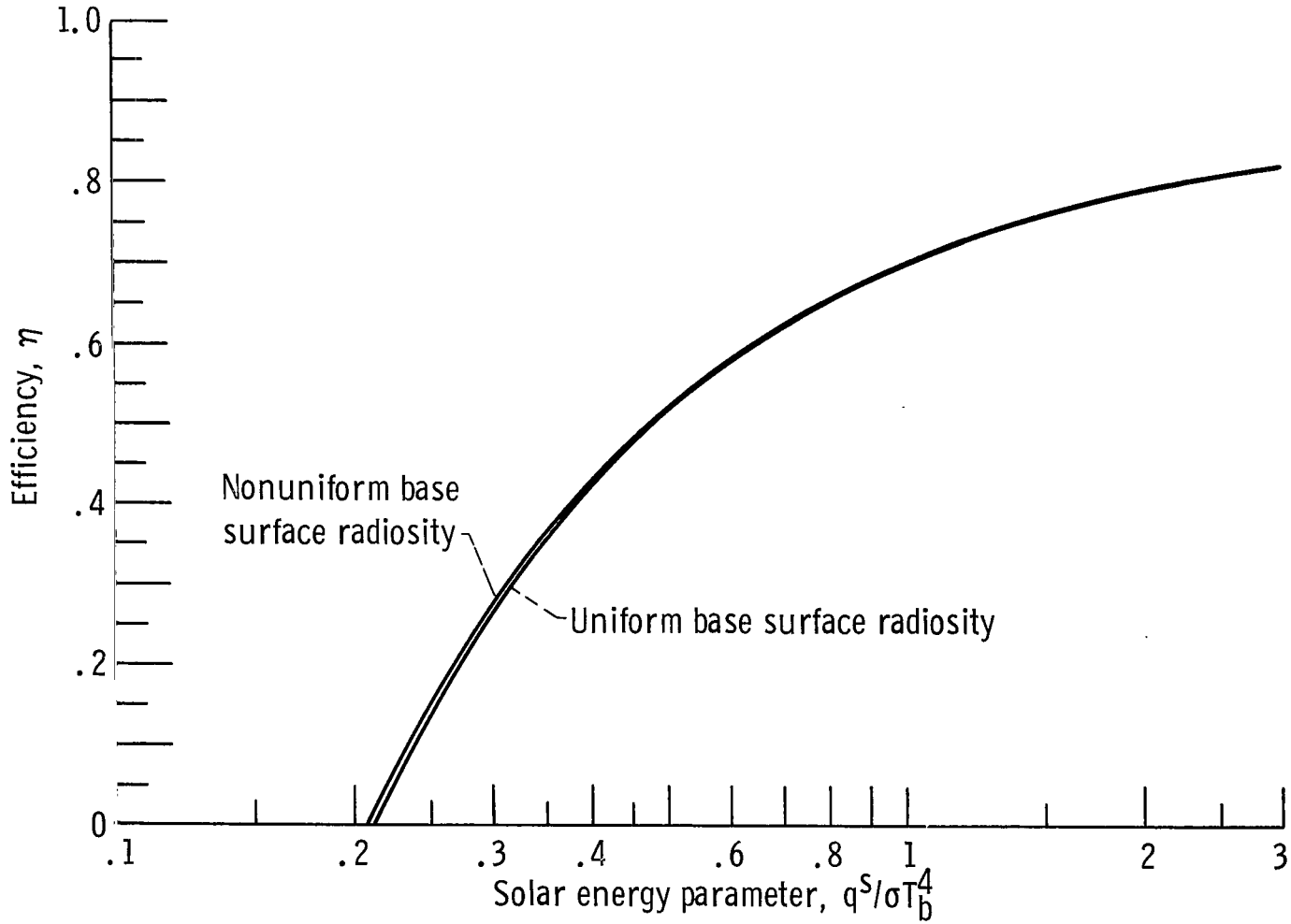

Figure 17. - Effect of base surface radiosity variation. Emittance $\epsilon = 0.5$; radiation-conduction parameter N = 20; depth-diameter ratio L/d = 5.

08U 001 58 51 3DS 71118 00903
AIR FORCE WEAPONS LABORATORY /WLOL/
KIRTLAND AFB, NEW MEXICO 87117

ATT E. LOU BOWMAN, CHIEF, TECH. LIBRARY

"The aeronautical and space activities of the United States shall be conducted so as to contribute . . . to the expansion of human knowledge of phenomena in the atmosphere and space. The Administration shall provide for the widest practicable and appropriate dissemination of information concerning its activities and the results thereof."

—NATIONAL AERONAUTICS AND SPACE ACT OF 1958

NASA SCIENTIFIC AND TECHNICAL PUBLICATIONS

TECHNICAL REPORTS: Scientific and technical information considered important, complete, and a lasting contribution to existing knowledge.

TECHNICAL NOTES: Information less broad in scope but nevertheless of importance as a contribution to existing knowledge.

TECHNICAL MEMORANDUMS: Information receiving limited distribution because of preliminary data, security classification, or other reasons.

CONTRACTOR REPORTS: Scientific and technical information generated under a NASA contract or grant and considered an important contribution to existing knowledge.

TECHNICAL TRANSLATIONS: Information published in a foreign language considered to merit NASA distribution in English.

SPECIAL PUBLICATIONS: Information derived from or of value to NASA activities. Publications include conference proceedings, monographs, data compilations, handbooks, sourcebooks, and special bibliographies.

TECHNOLOGY UTILIZATION PUBLICATIONS: Information on technology used by NASA that may be of particular interest in commercial and other non-aerospace applications. Publications include Tech Briefs, Technology Utilization Reports and Technology Surveys.

Details on the availability of these publications may be obtained from:

SCIENTIFIC AND TECHNICAL INFORMATION OFFICE

NATIONAL AERONAUTICS AND SPACE ADMINISTRATION

Washington, D.C. 20546